UNIVERSIY OF OSLO
Department of Chemistry

Yttrium Doped Barium Zirconate: Electrical Properties and Electrodes

Thesis of the Master of Science degree in Materials, Energy and Nanotechnology

Tobias Sass

June 2013

Preface

This thesis concludes the work of the Master of Science degree under the program for *Materials Science and Nanotechnology*, with focus on material chemistry at the Department of Chemistry, University of Oslo. The experimental work was carried out at the Center for Materials Science and Nanotechnology (SMN) in the period of August 2011 until June 2013.

I would particularly like to thank my supervisors Professor Truls E. Norby and co-supervisor Ragnar Strandbakke for enthusiastic discussions, and practical support in the lab.

I am very grateful for the help and support of the research group, especially Anna Magraso and Harald Fjeld Collaboration and discussions especially about technical issues were always fruitful with Harad whether in working time or over a "fredags øl".

Last but not least I would like to thank Stephan Winter for his endless patience when giving my thesis its final touch and my girlfriend for encouraging me after never-ending working days. And of course, I thank my mom and dad for the genetic basics and financial support.

University of Oslo, June 2013

Tobias Sass

Abstract

Studies of Y-doped barium zirconate (BYZ) have shown superior proton conductivity characteristic promising for its use as an electrolyte in a proton conducting solid oxide fuel cell. BYZ combines chemical and thermo stability with high bulk conductivity. Notwithstanding the high resistance of the grain boundary still remains as a challenge and is not yet solved.

The electrolyte BYZ adjusted with three different yttrium concentrations (10%Y=BYZ10, 15%Y=BYZ15, 20%Y=BYZ20) was sintered and subsequently characterized by electrochemical impedance spectroscopy. The analysis revealed a shift in activation energies at temperatures approximately 450°C, with high temperatures assigned to electron holes and low temperatures to proton conducting. This was further emphasized with pO_2- and pH_2O-dependencies. The total conductivity was similar for BYZ10 and BYZ20 which was most likely due to ratio of grains in the sample. BYZ10 compensated lower conductivity with bigger grains compared to BYZ20. BYZ15 showed the lowest total conductivity, however BYZ15 had the highest specific grain boundary conductivity.

The compatibility of $LaSrMnO_3$ (LSM), $La_{0.75}Sr_{0.25}Cr_{0.5}Mn_{0.5}O_{3-\delta}$ (LSCM) and $LaCrO_3$ with BYZ20 +2 wt%NiO was tested. The LSCM electrode was tested with a 2-electrodes 4-wire setup impedance measurement with varying temperature, oxygen and water vapour pressure. Experiments revealed a polarization resistance of the middle frequencies of $3.86\Omega cm^{-2}$, which is well in line with reports from literature comparison an in range of oxygen diffusion on the electrode surface to the three phase boundary. The low frequency range was determined as the adoption/desorption of oxygen at the electrode surface. This was the rate limiting process with a polarization resistance of $6.83\ \Omega cm^{-2}$. To lower the total polarization resistance, surface solution to be exploited are –pre-coating and further mechanical engineering.

Table of Contents

1 Introduction

1.1 Motivation and background

Worldwide the consumption of energy is rising because of increased demands from stationary applications, like power plants, but also for portable use, like in many electronic devices. Fossil fuel is currently the primary source for this energy. The product is distributed globally and thus highly available, easy accessible and the production costs are low. A rough estimation is that the global energy consumption will increase more than 50% until 2030 and that fossil fuel will cover over 80% of the energy demand.

However, the total resources of fossil fuel are not endless and the costs of its uses as source of energy are among others a high emission of carbon dioxide (CO_2) pollution. Combustion of fossil fuels, coal, natural gas and oil for energy (industry and electricity) and transport brings along the emission of carbon dioxide, and other harmful elements, for example sulphur (S). The increasing pollution of the environment with the greenhouse gas CO_2 essentially began with the industrial revolution at the end of the 18^{th} century. Since 1750 approximately 356 billion metric tons of carbon dioxide has been released to the atmosphere of which half of the fossil fuel emissions have occurred since 1980s [1]. This increased content of CO_2 in the atmosphere is the main culprit for the constantly rising effects summarised as “global warming” The change of climate on a global scale has serious consequences ranging from temperature increases to changes in precipitation pattern, rising sea levels and desertification, heavy floods and drought periods. The emission of sulphur dioxide from burning coal leads to formation of sulphuric and

sulphurous acid in the atmosphere. As a result acid rain will occur and this leads to among others to leaching of rare earth metals polluting rivers with aluminium or marquee complexes.

Renewable energy that is energy from wind, sunlight or geothermal heat can be an alternative when source of storage, e.g. in batteries are better developed. In principle batteries can the provide energy like a combustion engine and thus can also be used in mobile devices like cars. They using chemical stored energy and converting it directly to electricity, without wasting thermal energy. However, due their limited storage capacity and their efficiency as energy source is relatively small also because the density of energy storage is relatively low and the storage costs of the technology are expensive. Notwithstanding, energy production, from fossil or renewable sources and subsequent storage always have great losses of energy hence a primary goal for any future energy concept would be to combine generation and storage of energy. When energy is to be stored, then storage in form of hydrogen produced from renewable energy resources (biomas fermentation, Methanol, electrolysis, algae) is a future alternative provided that transport and storage is made easier and more cost effective.

The conversion of hydrogen into energy is achieved by use of fuel cells which essentially are specific types of galvanic elements. Fuel cells can convert chemically stored energy into electricity and have a wide field of application. They can replace batteries and combustion engines with the additional environmental benefit from using hydrogen (H_2) and oxygen (O_2) as energy sources. The end product of all processes is water (H_2O), heat, and electricity while CO_2 pollution does not occur.

A number of fuel cells exist (AFC, DMVC, MCFC, PAFC) of which the high temperature fuel cells are subject of this thesis. Two types exist, the oxygen ion conducting fuel cells (SOFC) and the proton conducting fuel cells (PC-SOFC). The SOFC technology so far is further advanced however, PC-SOFC has the highest theoretical effects and can be operated by lower temperatures than SOFC. In theory, PC-SOFC has the most promising future applications but despite the great potential challenging task lie ahead. First of all, to compete with traditional power production methods the efficiency of energy production has to be increased. The main issue here is to address the chemical potential which currently is not exploited appropriately. To further improve

the efficiency of the fuel cells, the electrochemical resistance has to be lowered. This applies for both the electrolyte and the electrode. Furthermore, chemical and mechanical forces need to be considered. Physical stresses due to thermal expansion can cause cracks and thereby destroying the electrolyte or electrode. Oxidising and reducing atmospheres impact the chemical stability of materials in particular at high temperatures. Chemical reactions, with sulphur or CO_2, can over time lead material deterioration. And, some electrolytes have particularly low conductivity and the entire electrochemical processes are not well understood. Thus fundamental research is necessary to enhance the understanding of the proton transport processes from reaction point to reaction point.

Research on new materials is important, but established systems, like fuel cells based on barium zirconate ($BaZrO_3$) also can be further investigated to improve our understanding of the fundamental mechanisms. Studies of new electrode materials, based on both real and general reaction systems allow the estimation of reaction rate determining processes and an evaluation of the surface potential of electrode materials. This is in particular significant for ion transport, catalytic effects and reduction potential.

Production of lab scale PC-SOFC is still in its early stages and because of production constraints, the full potential of PC-SOFC is not yet exploited. The production of $BaZrO_3$ is most critical because Barium zirconate doped with yttrium shows the highest known proton conductivity and has the additional features of high chemical stability within the required temperature range.

1.2 Aim and methods of the investigation

The use of yttrium doped barium zirconate as an electrolyte shall be investigated. Because of the challenging sintering properties of this material a comparative analysis of two different sintering processes will be conducted. The first one is a glycine-nitrate combustion synthesis process without sintering aid while in the second method a sintering aid will be introduced in a solid state reaction sintering process with 2wt% nano NiO powder added to reach high density at low sintering temperatures.

Barium zirconate will be investigated with three different yttrium concentrations, $BaZr_{0.8}Y_{0.2}O_{3-\delta}$ (BYZ20), $BaZr_{0.85}Y_{0.15}O_{3-\delta}$ (BYZ15), $BaZr_{0.9}Y_{0.1}O_{3-\delta}$ (BYZ10). To evaluate the effect of the sintering method, grain size will be determined using scanning electron microscope and EDS-analyses to assess the homogeneity of the internal structures.

The main focuses of the thesis are investigations of conductivity changes in relation to the level of yttrium doping. This conductivity of the electrolyte is an important criterion for general assumptions on the use of SOFC. The main tool for this evaluation is impedance spectroscopy which permits a differentiation between bulk and grain boundary conductivity. This is relevant for delineation and definition of rate limiting effects.

For the electrode, three cathode materials will be chosen to study the compatibility with BYZ20 + 2wt% NiO as electrolyte for proton conducting SOFCs. The electrode will be characterised by visual inspection and by determining its electrochemical properties. Temperature, oxygen- and water vapour pressure dependencies will be determined to characterize the reaction steps and to define rate limiting processes. The performance data obtained for the cathode will be critically evaluated in light of available literature.

2 Theory

Most of the defect chemistry and conductivity theory is based on Defects and Transport in Crystalline Solids by Kofstad and Norby [2], while other references are given in the text.

2.1 Electrical conductivity

Electrically charged species of type i (as an example $OH_o^{\cdot}$) with charge $z_i e$, in an electrical field, E, will be affected by the force, F, which is proportional to charge and field. The force is the reason for transportation of charge carriers and affects the current density:

$$i_i = z_i e c_i u_i E = \sigma_i E \tag{2.1}$$

with the concentration, c_i and mobility u_i of the species i, contributing to the charge carrier conductivity σ_i.

The Nernst-Einstein equation (2.2) describes the relation of the charge carrier mobility and conductivity to the self-diffusion coefficient.

$$D_i = \frac{u_i kT}{z_i e} = \sigma_i \frac{kT}{c_i (z_i e)^2} \tag{2.2}$$

This relationship applies solely for jumping processes, with an activation energy ΔE_a. The temperature dependency of this is related to, σ_0, the pre exponential factor of the following equation:

$$\sigma_i = \frac{\sigma_0}{t} exp\left(-\frac{\Delta E_a}{RT}\right) \quad (2.3)$$

where ΔE_a is the sum of ΔH_m and ΔH_f, transport and formation enthalpy, respectively. The activation energy may be derived from the Nernst-Einstein relation by estimating the slope of a natural logarithm of conductivity times temperature versus inverse temperature, Arrhenius plot $\left(ln(\sigma_i T)\ vs.\frac{1}{T}\right)$.

Materials consist often of various species that contribute to the conductivity. The total conductivity σ_{total}, is the sum of all partial conductivities σ_i:

$$\sigma_{total} = \sum \sigma_i \quad (2.4)$$

The charge transport is often dominated by only one of the charge carriers, while other carriers can have negligible concentrations. In Y-doped barium zirconate the charge carriers can be protons, oxygen vacancies or electron holes under oxidising conditions. In the given atmospheric condition of wet air, and temperatures below 500°C protons will be the main charge carrier, and electron holes and oxygen vacancies can be neglected.

2.1.1 Brick layer model

To calculate the specific grain boundary conductivity the brick layer model is used. This model assumes the cubic grains, with grain boundaries serially and parallel orientated. This is illustrated in Figure 2.1, where D is the length of the cubic bulk grains, δ the average thickness of the grain boundaries and L the thickness of the sample. The brick layer model associated the bulk and grain boundaries in parallel to the bulk as one semicircle at the heights frequencies in the Nyquist-plot. This is expressed by formula (2.5) [3]. The middle to low frequency arc is associated to the grain boundaries which are orthogonal to the way the current travels. This specific conductivity is expressed by formula (2.6).

$$\sigma_1 = \frac{2\delta}{D}\sigma_{Gb} + \sigma_{bulk} \tag{2.5}$$

$$\sigma_2 = \frac{D}{\delta}\sigma_{Gb} \tag{2.6}$$

In cases, where $\sigma_{bulk} > \sigma_{gb}$ and material has a typical structure $\delta << D$ the equation (2.5) can be reduced to equation (2.7). The current flow will follow the grain interior if possible, and avoid the grain boundaries because of their higher resistance. The current just passes through the grain boundaries when moving from grain to grain. The bulk specific conductivity (2.5) can then be written as:

$$\sigma_1 = \sigma_{bulk} \tag{2.7}$$

The specific grain boundary conductivity (2.6) is proportional to the thickness of the grain interior by δ/D. Since the dielectric constant of the bulk and grains boundaries is approximately the same, the following equation can be given:

$$\frac{\delta}{D} = \frac{C_{bulk}}{C_{Gb}} \tag{2.8}$$

where C_{bulk} and C_{gb} is the capacity for bulk and grain boundary, respectively. Combining now formula (2.6) with (2.8), the specific grain boundary conductivity can be calculated from impedance measurements by [4]:

$$\sigma_{sp.Gb} = \frac{C_{bulk}}{C_{gb}}\sigma_{Gb} \tag{2.9}$$

The bulk and grain boundary capacitance can be calculated form formula (2.23).

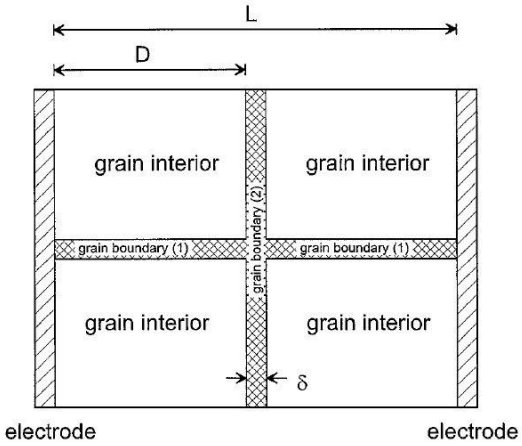

Figure 2.1: Brick layer model, simple illustration of the brick layer model with grain interior, parallel and serial grain boundaries [3].

2.2 Space charge theory

As the inspiration of this chapter the theories of De Souza [5] and Guo et al. [6] were used. Other references are listed in the text.

At the grain boundary structural differences from the bulk will appear. In this area the crystal lattice of the grains will adjust to each other, to reduce the crystallographic mismatch. This area is called grain boundary core. These structural differences to the bulk can be described as excess or deficit of ions or charged point defects. Occurrences of these defects are related to the differences of Gibbs formation energy in the bulk and grain boundary. The grain boundary could be either negatively or positively charged. Further it will be supposed that the core is positively charged, which is p-charged as shown in Figure 2.2 . To charge compensate the positive core, negative charge will accumulate on both sides of the grain boundary. The area with accumulated charges in the grain boundary region is called space charge layer. From an electrical point of view the space charge layer is a part of the grain boundary, however from a structural point of view, it is part of the bulk.

2.2.1 Electrochemical potential

The electrochemical potential for a mobile defect is given by:

$$\eta_j(\mathrm{x}) = \mu_j^0 + k_B T ln c_j(x) + Ze\varphi(x) \tag{2.10}$$

where μ_j^0 is the standard electrochemical potential and Z the effective charge. $c_j(x)$ and $\varphi(x)$ is defined as concentration of charge carriers and electrostatic potential at the distance x form the charge core, respectively . The electrochemical potential for this defect is given by:

$$\eta_j(\infty) = \mu_j^0 + k_B T ln c_j(\infty) + Ze\varphi(\infty) \tag{2.11}$$

At equilibrium conditions $\eta_j(\mathrm{x}) = \eta_j(\infty)$, the electrostatic potential can be written as:

$$\Delta\varphi(\mathrm{x}) = \varphi(\mathrm{x}) - \varphi(\infty) = \frac{kT}{Ze} ln \frac{c_j(\infty)}{c_j(x)} \tag{2.12}$$

The reorganization of equation (2.12) results in the concentration ratio to the electrochemical potential.

$$\frac{c_j(\infty)}{c_j(x)} = exp\left(\frac{Ze\Delta\varphi(\mathrm{x})}{kT}\right) \tag{2.13}$$

The Schottky barrier height is given by equation (2.14) and is the potential at the intercept between core and space-charge layer, relative to the grain interior [7].

$$\Delta\varphi(0) = \varphi(0) - \varphi(\infty) \tag{2.14}$$

The ration between the conductivity and space charge layer is shown by Kjølseth et al. [7] .

$$\frac{\sigma_{bulk}}{\sigma_{gb}} = \frac{exp\left(\frac{Ze\Delta\varphi(\mathrm{x})}{kT}\right)}{\left(\frac{2Ze\Delta\varphi(\mathrm{x})}{kT}\right)} \tag{2.15}$$

For the assumption that the bulk and grain boundary has the same mobility of charge carriers the activation energy can be estimated by an Arrhenius plot. In combination with formula (2.15) the differences between the activation energies can be calculated.

$$\begin{aligned}\Delta E_{a,gb} &= \Delta E_{a,gb} - \Delta E_{a,bulk} \\ &= (e\Delta\varphi(0) - k_B T)\left(1 + \frac{1}{T}\frac{dln\Delta\varphi(0)}{d\left(\frac{1}{T}\right)}\right)\end{aligned} \tag{2.16}$$

Now the activation energy of grain boundary conductivity has constitution of mobility, and the variation of the concentration of the charge carriers. These terms contain both the Schottky barrier height and the temperature dependency of the Schottky barrier height.

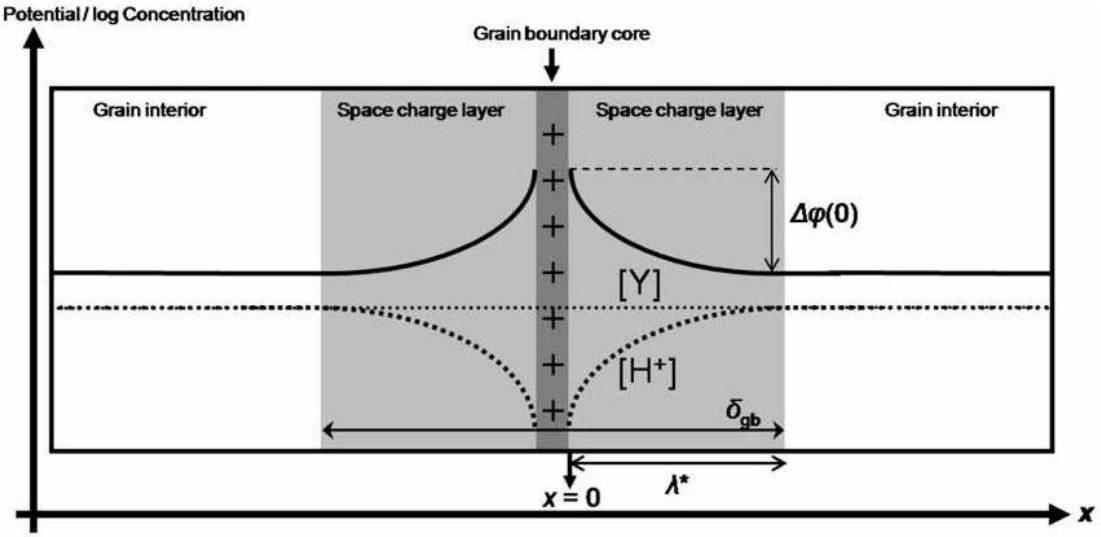

Figure 2.2: Space charge layer, schematic grain boundary consisting of a positive core charge compensated by two adjacent space–charge layers. Values of x are defined such that x=0 at the interface between the space–charge layer and the grain boundary core, while far into the grain interior x=∞. The dotted lines represent concentration profiles in the space–charge layer for the protons and acceptor dopant

under the Mott–Schottky approximation, while the unbroken line represents the potential profile. The Schottky barrier height potential difference is also indicated [7] .

2.3 Electrochemistry and impedance spectroscopy

Impedance spectroscopy is an important tool for characterizing the different conductivity components. This technique enables the identification of physical processes which appear in the bulk, grain boundary and electrodes.

2.3.1 Alternating current

In an alternating current AC, Voltage V, is represented by a sinus function which is characterized by its frequency, f, angular frequency ω, which can be express by 2πf, and the amplitude of V_0.

$$U = U_0 \sin(\omega t) \tag{2.17}$$

The product of ωt is called phase angle. An alternating current, *I*, which is has its origin in an imposed AC-voltage will have the same frequency, but can have different amplitude and phase angle.

$$I = I_o \sin(\omega t + \theta) \tag{2.18}$$

This phase shift, θ, occurs form the capacitance or inductance of the circuit, non-faradaic. Faradaic current occur when current depends on a oxidation or reduction mechanism of a species.

2.3.2 Resistance, capacitance, and inductance

An electrical resistor (or conductor) is a component through which charge carriers are transported. Number of charges, concentration and mobility of carriers are crucial for the conductance G, reciprocal to the resistance R. The current trough a resistor is independent of both the phase angle and the frequency due to ohmic nature. The relation between the voltage and the current is represented by Ohm's law.

$$R = \frac{U}{I} = \frac{U_0 \sin(\omega t)}{I_o \sin(\omega t)} = \frac{U_0}{I_o} \tag{2.19}$$

A capacitor consists of two conductors separated by an ideal resistor. The distribution between the maximal voltage and maximal current when applying alternating current is called capacitive resistance:

$$R_C = \frac{1}{\omega C} \tag{2.20}$$

where the capacitance is termed as C.

Inductors are ideal conductors without any resistance. As AC voltage passes through the conductor a magnetic field is created, which induces a new AC current U_L in another conductor. This new current has the same voltage, but in the opposite direction. Inductance, L, is measured with the unit Henry, H, and inductive resistance is $R_L = \omega L$.

2.3.3 Alternating current impedance and admittance in combined systems

AC impedance measurement has two components; one part is in phase, while the second part is out of phase. The part in phase is called the real part and is an obstacle for the charge transport. Once the voltage is shifted 90° in relative to the current it is out of phase. This gives rise to the imaginary part, the reactance, X. The total impedance, Z, given by Formula (2.21) consist of both parts and can be visualized in an two dimensional plot, Figure 2.3, where the real part is on the x-axis and the imaginary part on the y-axis:

$$Z = R + jX \tag{2.21}$$

where $j = \sqrt{-1}$.

The inverse impedance is the admittance Y. It has the same current to voltage ratio as the impedance. In this case the real part is called conductance G, and the imaginary component is termed susceptanc, B.

$$Y = \frac{1}{Z} = G + jB \tag{2.22}$$

2.3.4 Impedance spectrum

An impedance spectrum comprises a range of frequencies which correspond to the bulk, grain boundary and electrodes. Each response has a specific frequency region; bulk normally can be seen at high frequencies, followed by the grain boundary. The electrode is at low frequencies. This is illustrated in the Nyquist diagram (Figure 2.3). A capacitor performs best at high frequencies, while in the low frequencies range polarisation increases and causes higher impedance. This is shown in formula (2.21).

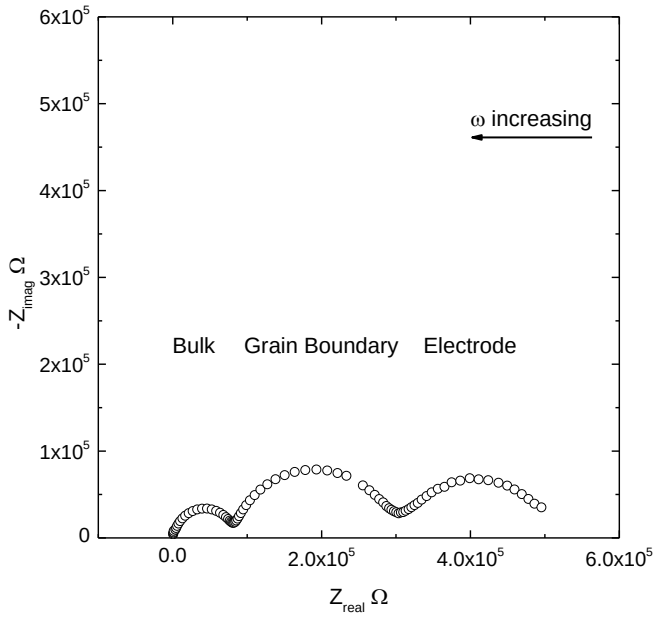

Figure 2.3: Nyqiust diagram, where the highest frequencies respond to the bulk, followed by Grain Boundary and Electrodes.

Each semicircle has pseudo capacitance, $C_{CPE,}$ calculated by formula (2.23), where R is the resistance in Ohm, Y_0 is the pseudo capacitance in farad and n is a non-dimensional parameter.

$$C_{CPE} = Y_0^{\frac{1}{n}} R^{\frac{1}{1-n}} \quad (2.23)$$

2.3.5 Constant phase element

Relaxation processes with a one single time coefficient are related to impedance spectra which contain perfect semicircles. However since these elements rarely appear, a slight overlap often occurs in practice. To counter the distribution of time constants caused by e.g. inhomogeneous samples, each semicircle will be assigned to a constant phase element, CPE, or Q. The CPE will have an admittance Y expressed in the following equation:

$$Y = Y^0(j\omega)^n \quad (2.24)$$

where the exponential n has an value between -1 and 1.
When n = 1, the CPE becomes an ideal capacitor and Y^0 becomes the capacitance, while in other cases where n = 0, the CPE is a pure conductor with Y^0 as the conductivity. When n = -1, the CPE stays a pure inductor and has Y^0 as inductance. Normally the value of n is somewhere in between.

Perfect systems are hard to reach. The reason for circles not being perfect mostly is due to the properties of the material. Structural differences e.g. size differences in grains, impurities or uneven thickness, contribute to distortion. Similarly, electrodes not being placed exactly on top of each other also will lead to anomalies of the system behaviour.

2.4 Equivalent circuit for electrodes

An impedance spectrum can be presented by various circuit elements. The bulk and grain boundary is often represented by a parallel connection of a resistor and a capacitor termed (RQ).

The electrode polarization is presented by two resistors. Those consist of variable equivalent circuits (EC), depending on the dominating processes and the general behaviour of reactants. In general, two resistors are chosen, one associated to the charge transfer R_{CT} and the other for diffusion resistance R_D. Each resistor has a specific capacitance and both capacitances are connected in parallel.

2.4.1 Randle's circuit

Electrodes are frequently be represented as a Randle circuit (Figure 2.4) which contains R_{CT} in series which an (RQ) element associated to the diffusion. Both elements are arranged in parallel to a capacitor.

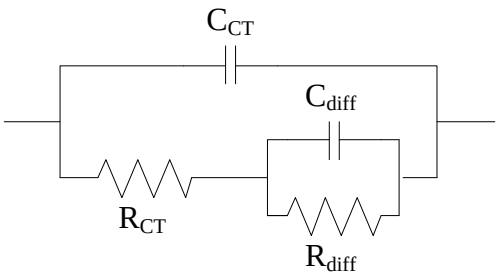

Figure 2.4: Randle circuit for electrodes, where R_{CT} is charge transfer and R_{diff} stands for charge diffusion

At the interface between the electrode and the electrolyte, an electrical double layer exists, termed double layer capacitance $C_{DL.}$ This layer comprises adsorbed species and typically consist only few atom layers, thus entailing a high capacitance. The resistance R_{CT}, responds to the activation barrier of both electrons and ions or to the electrode-electrolyte interface. The latter involves both chemical species as well as electrons.

Besides charge transfer, adsorption, gas phase diffusion and diffusion of species on the surface occur at the electrode. The rising capacitance is significantly higher than the double layer, which may be ascribed to chemical storage. In a Randle circuit this is represented by Q_D in a parallel connection to R_D. For infinitely large diffusion processes a blocking electrode is created that reduce the inner (R_DQ_D)-circuit to just Q_D.

In the context of this thesis, gas diffusion to the electrode is not considered. This is because gas diffusion does not involve activation energy an thus can be neglected int this work. The problem of gas diffusion at the electrode is not related to material properties and could be solved with improved engineering and construction.

2.4.2 Gerischer impedance

Electrochemical reaction as results of chemical reaction and followed by chemical reactions (CEC), are named Gerischer impedance [8]. Under certain conditions, is can be expressed by [9]:

$$Z = \frac{Z_0}{\sqrt{k + j\omega}} \tag{2.25}$$

where, *k* is the effective transfer rate of the chemical reaction.

Atangulov and Murigin [10] achieved a Gerischer impedance response for a gas electrode, characterized by limited a adsorption and surface diffusion. Other studies applied the Gerischer-impedance on porous mixed electrons and oxygen conducting perovskites [11].

$$K_a = \frac{1}{(Y_0 R_{DC})^2} \tag{2.26}$$

As shown in formula (2.25) , the Gerischer impedance can be calculated even at DC conditions. This circuit element therefore fits better to low frequency parts than other circuit elements.

2.5 Defect chemistry

Materials are built up of atoms or atomic groups, which are arranged in crystal lattices. In theory, the perfect crystal will solely exist at a temperature of 0 K. At higher and thus more realistic temperatures atoms deviate from the lattice position and form defects. Vacancies, substitute atoms, or interstitial atoms are some of the point defects. They influence the material properties, because of the different size and/or charge ratios compared to the original atoms. One, two or

three dimensional defects results in point, line, or secondary phases, respectively, but electronic defects in form of electrons and electron holes can also occur. In defect chemistry, the Kröger-Vink notation [12] describes the conventions used for electric charge and lattice position of point defects in crystals. It is one of the most applied notations.

Table 2.1: Kröger-Vink notation of point defects [12].

Defects	Notation
Electrons	e'
Electron holes	$h^{\cdot}$
Oxygen vacancies	$v_O^{\cdot\cdot}$
Yttrium on Zirconia site in BYZ	Y_{Zr}''

2.5.1 Defects in Barium Zirconate

The various of oxygen content, pO_2, can influence the material to form defects. One example is the formation of oxygen vacancies, $v_O^{\cdot\cdot}$, and electrons, e', as described in formula (2.27).

$$O_O^x = v_O^{\cdot\cdot} + 2e^{'} + \frac{1}{2}O_{2(g)} \tag{2.27}$$

With $v_O^{\cdot\cdot}$ as a effective doubly charged oxygen vacancy.

Further, metal vacancies can be created by removing the metal (2.28) or metal oxide (2.29). This applies especially for high temperatures, and with the requirement of at least one volatile component that is expected to evaporate.

$$Ba_{Ba}^x = v_{Ba}'' + 2h^{\cdot} + Ba_{(g)} \tag{2.28}$$

or

$$Ba_{Ba}^x + O_O^x = v_{Ba}'' + v_O^{\cdot\cdot} + BaO_{(g)} \tag{2.29}$$

These tow equations are examples on creation of metal vacancies in barium zirconate.

Barium oxide (BaO) has a low vapour pressure at sintering temperatures about 1500°C, and will evaporate from the sample, which will create barium vacancies and oxygen vacancies already in the sintering process, according to equation (2.29). In order to minimize this effect, sintering can be done in BaO containing atmosphere. However, the initial vacancy formation while sintering cannot be fully avoided [13].

2.5.2 Hydration

Some perovskites, such as barium zirconate, show a negative hydration enthalpy. In wet atmospheres, protons will be the majority defect [14]. The formation of protons is dissociative with the adoption of water. Hydration can be described by formula (2.30) where protons and vacancies are in equilibrium.

$$O_O^x + v_O^{\cdot\cdot} + H_2O(g) = 2OH_O^{\cdot} \qquad (2.30)$$

Two hydroxide ions are formed on the oxygen site, which provides an effective positive charge. The maximum water uptake then depends on the amount of oxygen vacancies and their hydration thermodynamic.

Furthermore, the existence of holes, $h^{\cdot}$, should be considered. In dry conditions and temperatures over 750°C the material creates holes (Formula (2.31)). As well known, this reaction shifts to the left at lower temperatures due to the high entropy, which accrues a large band gap and low electronic conductivity [15].

$$v_O^{\cdot\cdot} + \frac{1}{2}O_2(g) = O_O^x + 2h^{\cdot} \qquad (2.31)$$

2.5.3 Doping

As mentioned above, oxygen vacancies play a critical role for proton conductivity. To create more vacancies, doping with other species is introduced. In an acceptor-doped barium zirconate, one possibility is the replacement of Zr^{4+} with Y^{3+} ions. The charge compensating defect results in the creation of oxygen vacancies (2.32).

$$Zr_{Zr}^{x} + O_{O}^{x} + Y_2O_3 \leftrightarrow 2Y_{Zr}' + v_{O}^{\cdot\cdot} + 2ZrO_2 \qquad (2.32)$$

Doping with yttrium has different impacts, depending on the solubility ability limit. Below this threshold, the dopant concentration is constant and independent from oxygen pressure or temperature, while concentrations above the solubility threshold lead to formation of secondary phases.

2.6 Concentration of defects

The concentrations of different kinds of defects are depending on partial pressure of oxygen and the water vapour. This is displayed in the Brouwer-diagram (Figure 2.5and Figure 2.6). Depending on the availability of water or oxygen, equation (2.27) and (2.30) can be shifted to the right or left. As results the pO_2 dependency and pH_2O dependency can be visualised in Figure 2.5 and Figure 2.6, respectively.

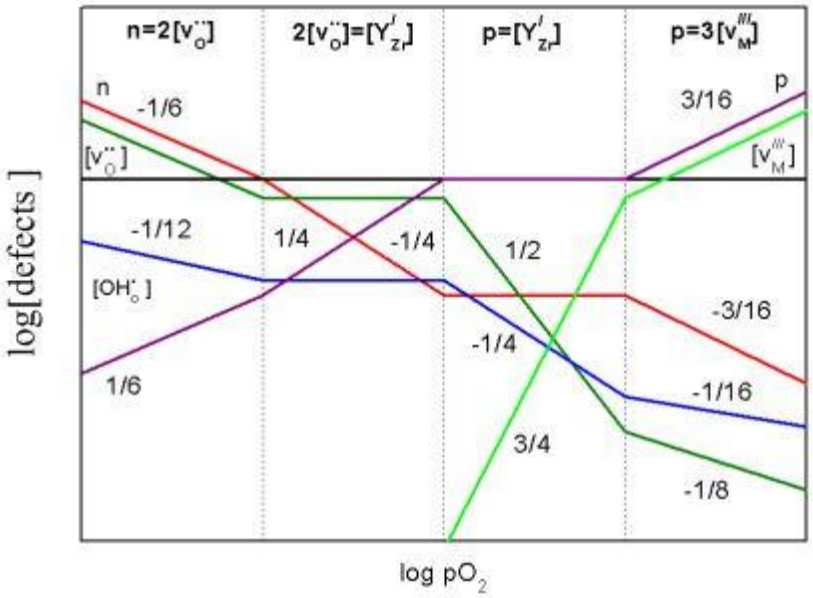

Figure 2.5: pO2-dependencies, different defect constriction as function of pO_2

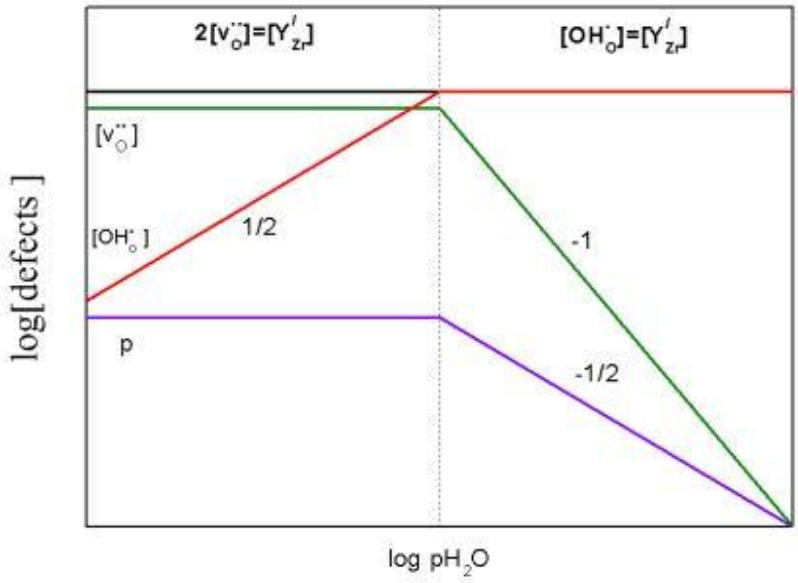

Figure 2.6: pH_2O-dependencies, different defect constriction as function of pH_2O

2.7 Electrode theory

One of the most commonly used models to describe the performance of electrodes was developed by van Heuveln and Bouwmeester [16].

The performance depends on adsorption, diffusion and charge transport. The mechanisms are interdependent and the rate limiting process is defining the reaction rate.

One possible reaction path of SOFC is described by van Heuveln and Bouwmeester [16], where the total reaction on the electrode is:

$$O_{2(g)} + 4e^- \rightarrow 2O^{2-}_{electrode} \tag{2.33}$$

This equilibrium (2.33) is divided into 3 steps, where in this particular model the charge transfer is rate limiting while the mas transport is infinitely high [17].

$$O_{2(g)} + 2ad \underset{k_{des}}{\overset{k_{ad}}{\leftrightarrow}} 2O_{ad} \tag{2.34}$$

$$2\left(O_{ad} + e^- \underset{k_{O3}}{\overset{k_{r2}}{\leftrightarrow}} O^-_{ad}\right) \tag{2.35}$$

$$2\left(O^-_{ad} + e^- \underset{k_{O3}}{\overset{k_{r3}}{\leftrightarrow}} 2O^x_O + ad\right) \tag{2.36}$$

The notation ad stands for adsorption, des desorption, and k is the rate constant.

By using this model it is possible to identify features which are likely to reduce the effectiveness of the electrode; a) mass transport as limiting factor, b) charge transfer processes in combination with mass transport as limiting factors, and c) charge transport as the limiting factor. Each of this can be determined through oxygen dependency and impedance measurements. A quantitative analysis of impedance spectra can also be done by observing an induction loop at low

frequencies. While an induction loop can occur in case b) and c), it is absent in the scenario a). However this method cannot differentiate between case b) only charge transport or c) both mass and charge transport as the reaction limiting factors [18].

The oxygen reduction model developed by Jae-Dong Kim [19] can be used to estimate the transfer and surface diffusion of oxygen ions for LSM-YSZ stabilized composites. The oxygen reduction model for a SOFC is described in 5 steps [19]:

Table 2.2: Reaction model, displays the elementary reaction, rate equation and pO_2 dependency of SOFC.

	Elementary reaction	Rate equation	pO_2
Step 1:	$O_{2(g)} \rightarrow 2O_{ad}$	$r_1 = k_1 pO_2 - k_1' a^2 O_{ad}$	1/2
Step 2:	$O_{ad} + e^- \rightarrow O_{ad}^-$	$r_2 = k_2 aO_2 \exp(-\frac{fE}{2}) - k_2' aO_{ad}^- \exp(\frac{fE}{2})$	3/8
Step 3:	$O_{ad}^- \rightarrow O_{TPB}^-$	$r_3 = k_3 aO_{ad}^- - k_3' aO_{TPB}^-$	1/4
Step 4:	$O_{TPB}^- + e' \rightarrow O_{TPB}^{2\prime}$	$r_4 = k_4 aO_{TPB}^- \exp(-\frac{fE}{2}) - k_4' aO_{TPB}^{2-} \exp(\frac{fE}{2})$	1/8
Step 5:	$O_{TPB}^{2-} + v_O^{\cdot\cdot} \rightarrow O_O^X$	$r_5 = k_5 aO_{TPB}^{2-} - k_5'$	0

The notation k_i and k_i' are rates constants for the forward and backward reactions. Other notations used are f = F/RT where T is absolute temperature, R the gas constant and F the Faraday constant, express the electrode potential and the length of the three phase boundary between electrode and electrolyte.

By using the theory of Heuveln and Bouwmeester, He et al. [20] found differences int the effect of the oxygen partial pressure of an SOFC. The identical steps were also described but the pO2-dependencies varied between the steps.

2.8 Three phase boundary

On the cathode side the oxygen is reduced to O^{2-}. Typically, this reaction occurs at the electrode/electrolyte interface, where three phases the gas, electrons and ions meet [21]. The

three-phase (or triple-phase) boundary (TPB) is at the perimeter cathode material (α) and electrolyte phase (ϒ) along the gas phase (β). A Simplified description of this process is illustrated in Figure 2.7 and represents one of many oxygen reduction processes occurring at a SOFC cathode [21]. Oxygen molecules get adsorbed onto a solid surface and through catalytic reactions undergo reduction to ionic/atomic species (O^{n-}). Prior to complete reduction, oxygen has to be totally reduced, and transported to the electrolyte material along the surface interface or inside the electrode bulk. Here it is incorporated and forms O^{2-}. Each of these steps depends on the electrode and electrolyte material. However, the location of these processes and the rate limiting elements are only partly understood.

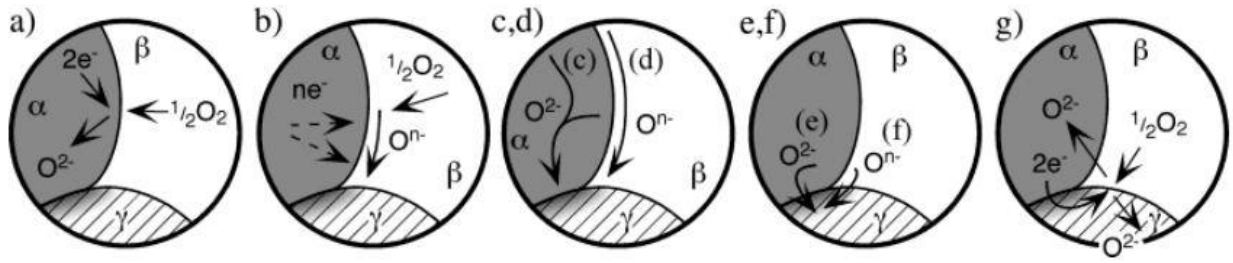

Figure 2.7: Different mechanisms for oxygen reduction in SOFC cathodes. Phases α, β and γ refer to the electronic phase, gas-phase and ionic phase, respectively. a) if mixed electron an ionic conducting oxygen goes into the bulk of the electronic phase; b) adsorption and reduction of oxygen on the electronic phase before surface diffusion; c) bulk or; d)surface and electrode bulk transport of O^{n-} and O^{2-}, respectively to the three phase boundary e) charge transfer of O^{2-} or f) combination of O^{n-} and e^-, respectively across the a/c interface; g) generation and transport of oxygen species which consist one or more of the previous mechanism [21].

The three-phase boundary has a 1 dimensional geometry. According to this, the performance of an SOFC is strongly dependent on its 1D geometric length. As a result research focuses on developing SOFC electrodes to insure the longest TPB possible particularly considering the microstructure of TPB to improve the performers of SOFC electrodes.

3 Literature

3.1 Background

Barium zirconate has a perovskite structure. Perovskites were first described by Gustav Rose in 1839, who found the first of these complex compounds in the Ural Mountains. He named those in honour of Russian discoverer and mineralogist Count Lev Alekseevich Perovski. In the same year, Christian Friedrich Schönbein investigated the electrolysis of water, which provided the fundaments of the invention by William Grove, the "voltaic battery", which from 1889 onwards is called the "Fuel Cell" [22].

The first perovskite was calcium titanium oxide ($CaTiO_3$), giving rise to the general structural formula ABO_3The first studies on pure barium zirconate were done in march 1930, basically to determine its melting point [23], but it took 13 more years to identify barium zirconate as a perovskite. Its space group and atom lattice was charted [24] and in 1951 electrical properties were such as the dielectric constant, ε_r, determined[25]. The proton conductivity in $BaZrO_3$ was discovered in Japan in 1981, in experiments to produce hydrogen from electrolyzing steam [26]. At the end of the second millennium, proton conducting experiments were also done with yttrium doped barium zirconate, and this finally opened the way to the hydrogen society [27].

3.2 Perovskite structure

Perovskite is generic name used for all oxides with the crystal structure ABO_3. In this form the A-cation is a metal with the charge +2 or +3 and the B-cation has the charge +4 or +3. In a unit cell, the A-cations are placed at the 4 corners, while the B-cations are in the centre of the square. Oxygen ions are placed in the middle of all surfaces, as shown in Figure 3.1.

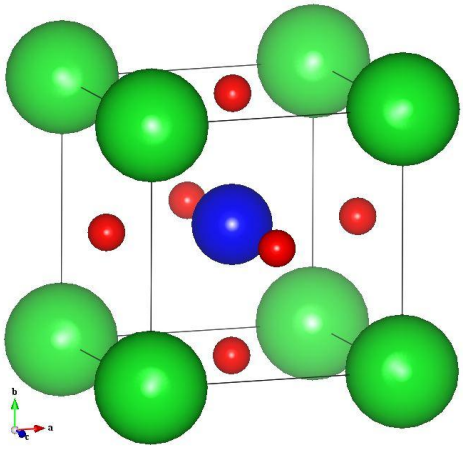

Figure 3.1: Unit cell of barium zirconate, where green = Barium, blue = Zirconia, and red = Oxygen

Undoped Barium Zirconate has a single-face symmetry with the space group Pm-3m and the lattice parameter of 4.1973Å. Yttrium doping changes the lattice parameter and with high doping concentrations the symmetry shifts from being cubic to tetragonal. The critical concentration for his alteration will be above 10 mole% yttrium. After its transition the space group will be P4mm and the lattice parameter a = 4.2413Å and c = 4.42259Å. When exceeding the threshold of more than 25 mole% Y-doping this will revert back to the cubic form [15].
The cubic crystal structure can vary from the perfect crystal through 3 main effects: 1. Size effects, 2. Charge compensating, 3. Jahn- Teller effects. The perfect cubic crystal has the lattice parameter, a, which is geometrically related to the ionic radius (r_A, r_B, og r_0).

$$a = \sqrt{2}(r_A + r_0) = 2(r_B + r_0) \tag{3.1}$$

The ratio between this to equation is called Goldschmit's tolerance factor, t, and is the basis to estimate the deformation of the lattice. In principle all bondings are ionic, but also strong ionic bondings can be considered to be correct.

$$t = \frac{(r_A + r_0)}{\sqrt{2}(r_B + r_0)} \tag{3.2}$$

For a perfect crystal t = 1, if the A-ion gets smaller, the t value will decrease. As a result of this, the BO_6 octahedron will tilt for filling the gap. As t gets even smaller, the structure will change form cubic to orthorhombic. The opposite will be t>1, for example with big A-cations and small B-catione. Then the octahedron is stabilized and the hexagonal structure is stable.

Y-doping rise creates of oxygen vacancies, as shown in section 2.5.3. The result is that B-ions get different oxidation states. Some will get a charge of +3 and some +4. Oxygen vacancies can form square pyramids. This formation of clusters is also known form other materials [28].

3.3 Hydration of Perovskites

Like described in section 2.5.2, protonic defects are created by uptake of water [29].

The hydration can be described thermodynamic by its standard Gibbs energy, enthalpy and entropy.

$$K_{hydr} = exp\left(-\frac{\Delta G^0_{hydr}}{RT}\right) = exp\left(\frac{\Delta S^0_{hydr}}{R}\right) \cdot \exp\left(-\frac{\Delta H^0_{hydr}}{RT}\right) = \frac{[OH_O^{\cdot}]^2}{[v_O^{\cdot\cdot}][O_O^X]p_{H_2O}} \quad (3.3)$$

Where K_{hydr} is the equilibrium constant and is related to the enthalpy and entropy, which defines the concentration ratio between protonic defects and oxygen vacancies. For a range of perovskite materials, this equation is exothermic, which means that protons are the dominating species at lower temperatures, while oxygen vacancies are predominate at high temperatures.

Studies done by Larring and Norby [30] showed that a range of perovskites and rare earth metals have en hydration entropies in between -120±40 J/molK, for loss of one mole of gas. The enthalpy however seems to be material specific. Kreuer [31] suggest that the increasing basicity of the corresponding oxides favour a more negative hydration enthalpy through the creation of strong OH-bonding. This is shown for selected perovskites are shown in Figure 3.2. The hydration enthalpy gets more negative with the change from Sr → Ba and Nb → Zr → (Ce, Er) occupying the A- and B-site, respectively.

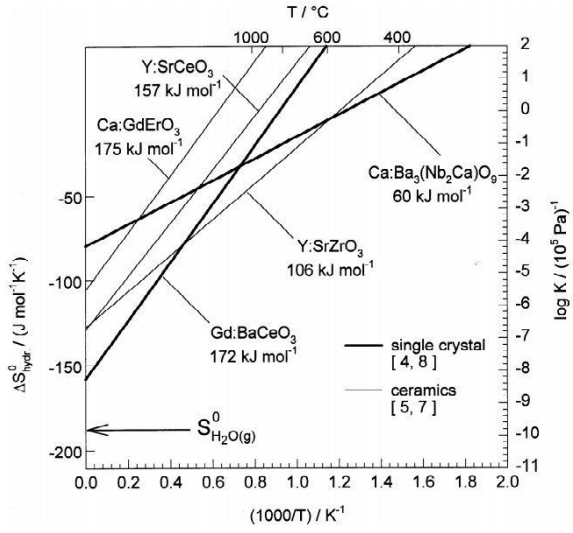

Figure 3.2: Logarithm of equilibrium constant for hydration enthalpy as a function of inverse temperature for some perovskite materials.

Later Kreuer showed also that the hydration enthalpy for acceptor doped perovskite decrease form titanates →niobates → zirconates → stannates → cerates with basicity [32]. A mathematical solution to estimate the hydration enthalpy was suggested by Norby [30]. Based on experimental data a quantitative correlation between hydration enthalpy and electronegativity differences of A- and B-cations was developed.

$$\Delta H_{hydr} = 400 \cdot \Delta X_{B-A} - 180 \qquad (3.4)$$

ΔX_{B-A} is the Allred-Rochow electronegativity and as suggested by Bjørheim [33] this absolute value $|\Delta X_{B-A}|$ must always be used. The correlation between the Goldschmidt tolerance factor and hydration enthalpies indicates that protons are stabilized by the structural distortions to a larger extent than oxygen vacancies.

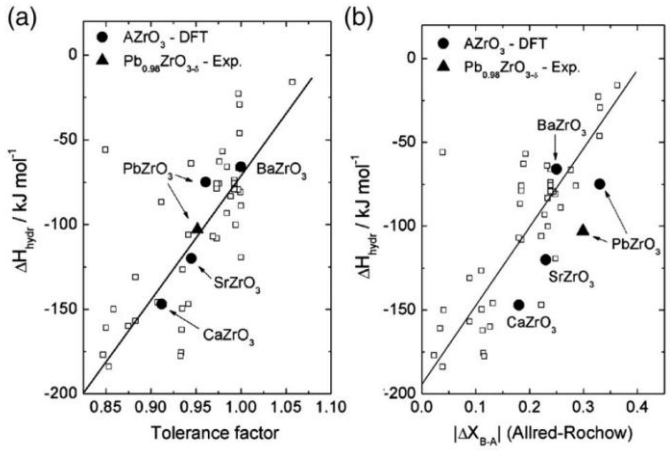

Figure 3.3: Experimental and calculated values for the hydration enthalpy, as (a) function of Goldschmidt tolerance factor and (b) absolute value of Allerd-Rochow electronegativity [33]

3.4 Stability

High proton conductivity combined with chemical stability has for a long time been a challenge[15]. As mentioned before more alkaline materials has higher proton conductivity, however is unstable when exposed to acid gases like CO_2 or SO_3. Considering a simple perovskite of type ABO_3 in an reacting with CO_2 the following reaction will occur: $ABO_3 + CO_2 = ACO_3 + BO_2$ [31]. For example is BaCeO3 which has high proton conductivity, but poor chemical stability will decompose in CO_2 enriched atmosphere [34]. In contrast, yttrium doped barium zirconate shows a high chemical stability against CO_2 atmosphere, and combines high proton conductivity with stability[32]. A study by Babilo [35] investigated $BaCeO_3$ and BYZ15 over a temperature range where weight increases was correlated with CO_2 uptake and material decomposition. Consequently it can be resumed, that resistance against CO_2 can improves durability of the electrolyte, and reduces the essential requirements of the atmospheric conditions.

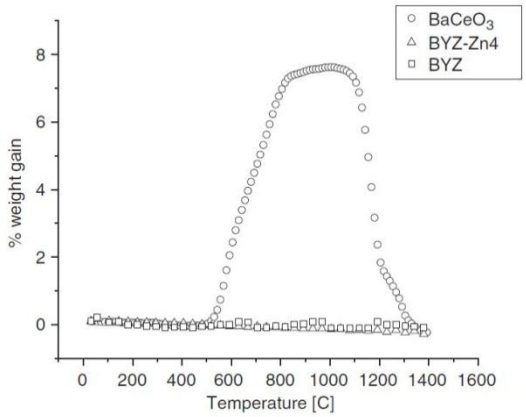

Figure 3.4: $BaZr_{0.85}Y_{0.15}O_3$ (BYZ), $BaZr_{0.85}Y_{0.15}O_3$ with 4 mole% ZnO (BYZ-Zn4) and $BaCeO_3$ weight changes in present plotted against temperature changes inCO_2 containing atmosphere [35].

3.5 Conductivity of the electrolyte

The first electrical characterisation of BaZrO3 was done at high temperatures, where only the total conductivity was measured. It was long believed that barium zirconate was a bad proton conductor because of its high bulk resistance. With the introduction of impedance spectroscopy at low temperatures this has changed and it became clear that resistance was because of the grain boundary and not related to bulk resistance. It is well known fact that barium zirconate is hard to sinter and therefore the grain sizes often are small. As a result, more grain boundaries will be present with negative consequences for total conductivity.

The change of activation energies observed at temperatures above 300°C were attributed to the loss of protons. Under this temperature the bulk activation energy was found to be 0.44eV which was later was confirmed by Kreuer et al. [29] who calculated an activation energy of 0.43eV using thermo gravity analyses. Using impedance spectroscopy it was also possible to determine the activation energy of the grain boundary for temperatures below 500°C which was 0.7-0.8eV (Bohn et al. [36]). In the same study it was found that protons are dominating the grain boundary conductivity under wet conditions, while electron holes dominate in dry conditions.

For higher temperatures the situation is somehow different. Since the grain boundary activation energy is higher than the bulk activation energy, the total conductivity becomes more and more

dominated by the bulk resistance. In wet atmospheres the conductivity is unaffected by the change of oxygen partial pressure, while in dry atmosphere the conductivity changes with pO2. As described in equation (2.31) dry atmospheres lead to creation of electron holes. Bohn et al concluded that in 10% yttrium doped barium zirconate electron hole conductivity supresses proton conductivity under oxidising conditions (pO2 < 10-5atm) while under reducing conditions protons are dominating and electrons can be neglected [37]. This defines $BaZr_{0.9}Y_{0.1}O_{3-\delta}$ as an almost perfect proton conductor.

A range of studies investigated proton conductivity in acceptor doped barium. These studies show a wide range of conductivity for this material. Kreuer et al. [29] suggested that this discrepancy is attributable can be the evaporation of barium during the sintering process. Studies show that a under stoichiometry of 3-4 mol% barium the conductivity is decreased by a factor of 2 [38]. Figure 11 shows some of the conductivity data obtained in independent studies.

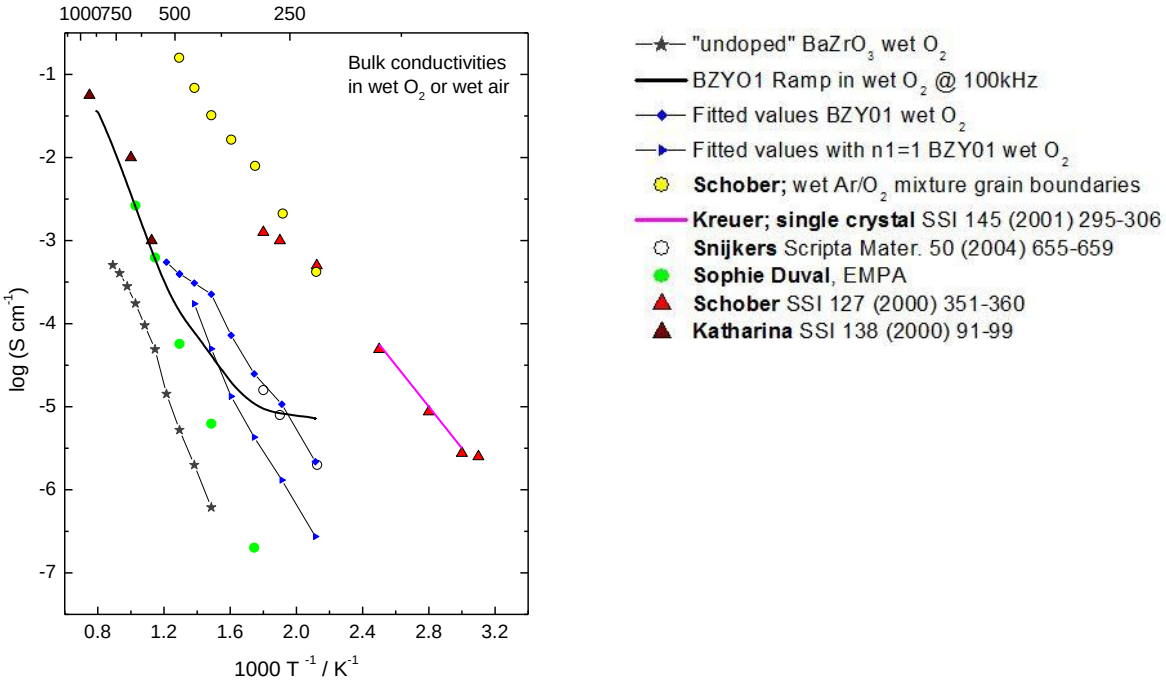

Figure 3.5: Overview of bulk conductivity of yttrium doped barium zirconate done in O_2 or air [39].

3.6 Grain boundaries in Y-doped BYZ

Several studies have shown that acceptor doped barium zirconate has a high specific grain boundary resistance. It was suggested by Kreuer [29] that the reason of high specific grain boundary resistance is correlated to the asymmetry between the grains. Newer investigations revealed that the concentration differences of defects and the emergence of space charge layers are responsible for low conductivity [5]. The theoretical dimension of the grain boundary can be estimated from the Schottky barrier height equation described in section (2.2).

They are two ways to improve the total grain boundary conductivity. The first one is to lower the number of grain boundaries which implements bigger grains, and the second one is to increase the transport properties across the grain boundary. The latter is very difficult to achieve because the transport mechanism is not fully understand and therefore methods to improve the specific grain boundary conductivity are not available. The improvement of grain size has been attempted by changing method of synthesis and by using of sintering aids such as NiO, ZnO.

The best overview over the properties of the grain boundaries is obtained by comparing activation energy and conductivity. Unfortunately, this is not easy because most reports refer to total conductivity rather than specific conductivity. Studies done by Babilo et al. [38] estimated a specific grain boundary conductivity of 4.4 10-6S/cm with an activation energy of 0.78eV. These values correspond to those reported by Bohn et al.[36] and Kjølseth [7]. Lower activation energies were reported by Iguchi, claiming that yttrium accumulates in the grain boundary core and thus lowers the Schotky height [40].

3.7 Oxygen side electrodes

Research on cathode was driven by the search of alternatives for platinum in SOFC application. Because most oxides are isolators, transition metal oxides as a low cost alternative to platinum were extensively studied form 1965 onwards. One of the first materials studied was $La_{1-x}Sr_xCoO_{3-\delta}$ (LSC) by Button and Archer. Short time after other materials with perovskite structure was studied and in 1973 one of today most studied electrode $La_{1-x}Sr_xMnO_{3-\delta}$ (LSM) becomes the impressive SOFC-electrode. To improve the performance further, the introduction

of bulk oxygen ion conducting electrodes with a more complex structure were developed. The first electrode with better kinetic properties than Pt in a temperature range of 1000-1100°C was $La_{1-x}Ca_xCoO_{3-\delta}$ which was found in 1981. Later the studies of some more general formula $La_{1-x}Sr_xMO_{3-\delta}$ (M = Cr, Mn, Fe, Co) were introduced [21].

From the list of available literature, 4 general lines of research can be deduced. The first concern those research groups studying the underlying theoretical issues (shown in section 2.7), several researchers groups are involved in the determination of polarization resistance, other with conductivity measurements and the fourth is dealing with fuel cell testing.

Studies by E.Quarez et al. [41] have determined the polarization resistance for LSM and LSCM of 4.3 cm^{-2} and 15.5Ωcm^{-2} in humidified air at 750°C, respectively. This study was done on La_6WO_{12} proton conducting electrolyte. The electrode material investigated in this study was $Ba_{0.5}Sr_{0.5}Co_{0.8}Fe_{0.2}O_3$ (BSCF) which under similar conditions and temperatures determined a polarization resistance of 9.7 Ωcm^{-2}. The explained the lower polarization resistance for LSM with higher oxygen conductivity in comparison to LSCM and a reaction phase between electrolyte and BSCF electrode.

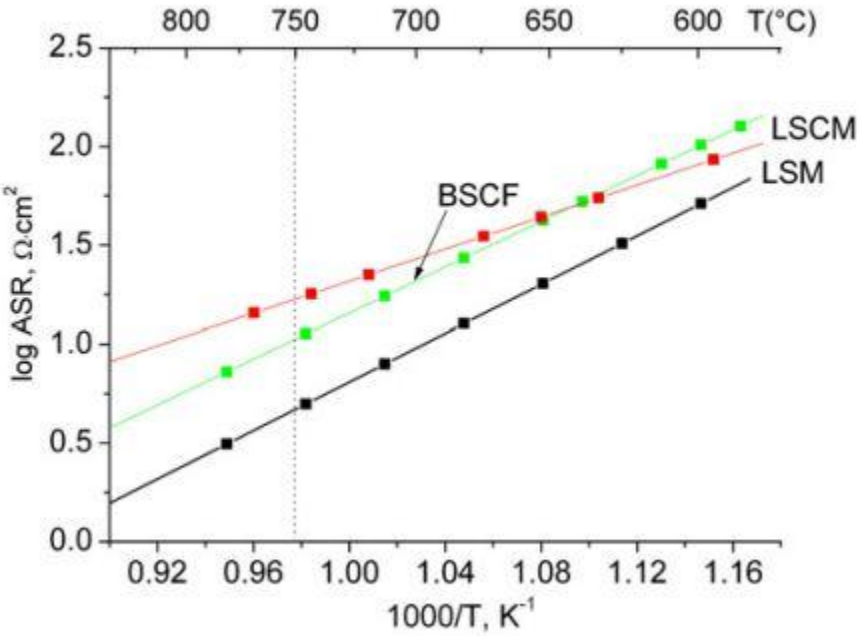

Figure 3.6: Temperature dependency of LSCM LSM and BSCF in wet air, measured in a half cell with proton conducting electrolyte [41].

Different studies were done with a wide range of electrodes and electrolytes. Recote et al. [42] investigated LSCF on $BaCe_{0.2}Zr_{0.7}Y_{0.1}O_{3-\delta}$ proton conducting electrolyte. The measurements were done in wet air, and the total resistance was divided in charge transfer resistance and adsorption/desorption polarization resistance. The values for the charge transfer resistance was $0.61\Omega cm^{-2}$, and the adsorption desorption resistance was estimated be $0.89\Omega cm^{-2}$.
Further the Figure 3.7 shows a representative overview of polarization resistance measured for different electrodes on diverse electrolytes.

Cathode material	Electrolyte	Cathode fabrication method	$p(H_2O)$ (atm)	R_p (Ω cm^2)
$LaCoO_3$	BCZY27	Infiltration into	0.01	0.11
		porous backbone	0.03	0.14
$Ba_{0.5}Sr_{0.5}Co_{0.8}Fe_{0.2}O_{3-\delta}$	$BaCe_{0.9}Y_{0.1}O_{3-\delta}$	Screen printing	0.03	~1.5
		Spray deposition	–	~0.5
$La_{0.6}Sr_{0.4}Co_{0.2}Fe_{0.8}O_{3-\delta}$	$BaCe_{0.9}Y_{0.1}O_{3-\delta}$	Screen printing	0.03	~6
	$BaCe_{0.9}Y_{0.1}O_{3-\delta}$	Painting of slurry	0.03	~7.9
$La_{0.58}Sr_{0.4}Co_{0.2}Fe_{0.8}O_{3-\delta}$	BCZY27	Spray pyrolysis	0.001	0.61
			0.03	0.89
		Infiltration into	0.001	0.63
		porous backbone	0.03	0.98
		Screen printed	0.01	0.8
$Pr_2NiO_{4+\delta}$	$BaCe_{0.9}Y_{0.1}O_{3-\delta}$	Screen printing	0.03	~1.5
$PrBaCo_2O_{5+\delta}$	$BaZr_{0.1}Ce_{0.7}Y_{0.2}O_{3-\delta}$	Spray deposition	–	0.73
$Y_{0.5}Pr_{0.5}BaCo_2O_{5+\delta}$	$BaZr_{0.1}Ce_{0.7}Y_{0.2}O_{3-\delta}$	Spray deposition	–	0.59
$Ca_3Co_4O_{9+\delta}$	$BaCe_{0.9}Y_{0.1}O_{3-\delta}$	Painting of slurry	0.03	2.2
$Ca_{2.7}La_{0.3}Co_4O_{9+\delta}$	$BaCe_{0.9}Y_{0.1}O_{3-\delta}$	Painting of slurry	0.03	~2.2
$La_{0.6}Sr_{0.4}Co_{0.2}Fe_{0.8}O_{3-\delta}/BaCe_{0.9}Yb_{0.1}O_{3-\delta}$ composite (1:1 by weight)	$BaCe_{0.8}Y_{0.2}O_{3-\delta}$	Painting of slurry	0.03	~1.1
$Pr_{0.58}Sr_{0.4}Fe_{0.8}Co_{0.2}O_{3-\delta}/BaCe_{0.9}Yb_{0.1}O_{3-\delta}$composite (60:40 by volume)	$BaCe_{0.9}Y_{0.1}O_{3-\delta}$	Screen printing	0.023	~1.2
$Pr_{0.58}Sr_{0.4}Fe_{0.8}Co_{0.2}O_{3-\delta}/BaCe_{0.9}Yb_{0.1}O_{3-\delta}$ composite (50:50 by volume)	$BaCe_{0.9}Y_{0.1}O_{3-\delta}$	Screen printing	0.023	~1.25
$Pr_{0.58}Sr_{0.4}Fe_{0.8}Co_{0.2}O_{3-\delta}/BaCe_{0.9}Yb_{0.1}O_{3-\delta}$ composite (40:60 by volume)	$BaCe_{0.9}Y_{0.1}O_{3-\delta}$	Screen printing	0.023	~1.4
$Sm_{0.5}Sr_{0.5}CoO_{3-\delta}$ (SSC)	$BaCe_{0.8}Sm_{0.2}O_{3-\delta}$	Infiltration of SSC in $BaCe_{0.8}Sm_{0.2}O_{3-\delta}$	–	0.21
$Sm_{0.5}Sr_{0.5}CoO_{3-\delta}/BaCe_{0.8}Sm_{0.2}O_{3-\delta}$ composite (55:45 by weight)	$BaCe_{0.8}Sm_{0.2}O_{3-\delta}$	Screen printing	–	0.67
$LSCF/BaZr_{0.5}Pr_{0.3}Y_{0.2}O_{3-\delta}$ composite	$BaZr_{0.5}Pr_{0.3}Y_{0.2}O_{3-\delta}$	Painting of slurry	0.03	0.157
$LSCF/BaZr_{0.7}Pr_{0.1}Y_{0.2}O_{3-\delta}$ composite	$BaZr_{0.7}Pr_{0.1}Y_{0.2}O_{3-\delta}$	Painting of slurry	0.03	~0.8

Figure 3.7: Shows a selection of cathodes on different electrolytes. The values are obtained in air by 600°C[43].

Figure 3.8 shows a selection of electrodes and there conductivity. For the usage of electrode it not only has to have a high conductivity but also a chemical stability and good catalytic effects.

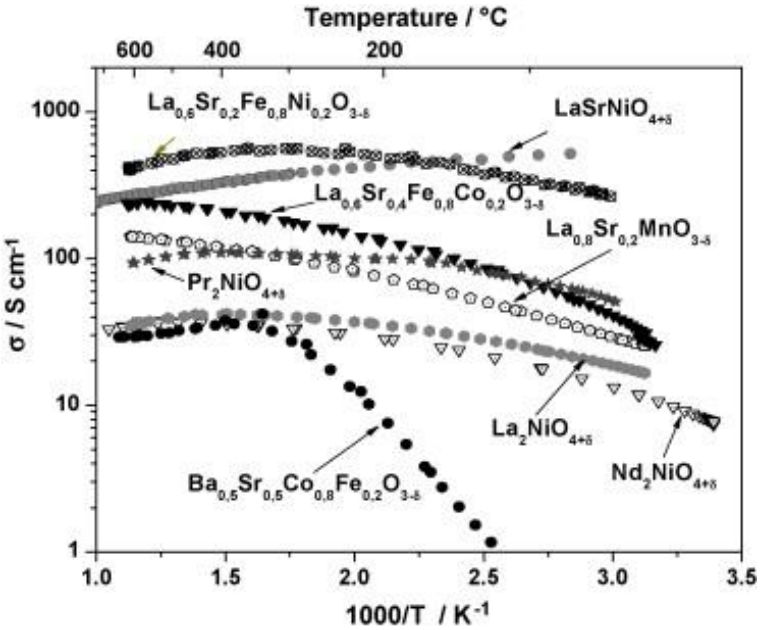

Figure 3.8: Selection of electrodes and there conductivity [44].

The best cathode performance today was achieved by Shao and Haile[45]. They used $Ba_{0.5}Sr_{0.5}Co_{0.8}Fe_{0.2}O_{3-\delta}$ (BSCF) in a oxide conducting cathode. BSCF was developed for the mediate temperature range for 500-700°C. The total polarization resistance was found to be $0.021\Omega cm^{-2}$ and the power output just above $1Wcm^{-2}$. Theoretical this material is one of the most promising materials at the cathode side. Further researches are concentrating on the stability of this material, because of the high degradation rate. Figure xx shows the power output in $mWcm^{-2}$ as function of the voltage-current density dependency.

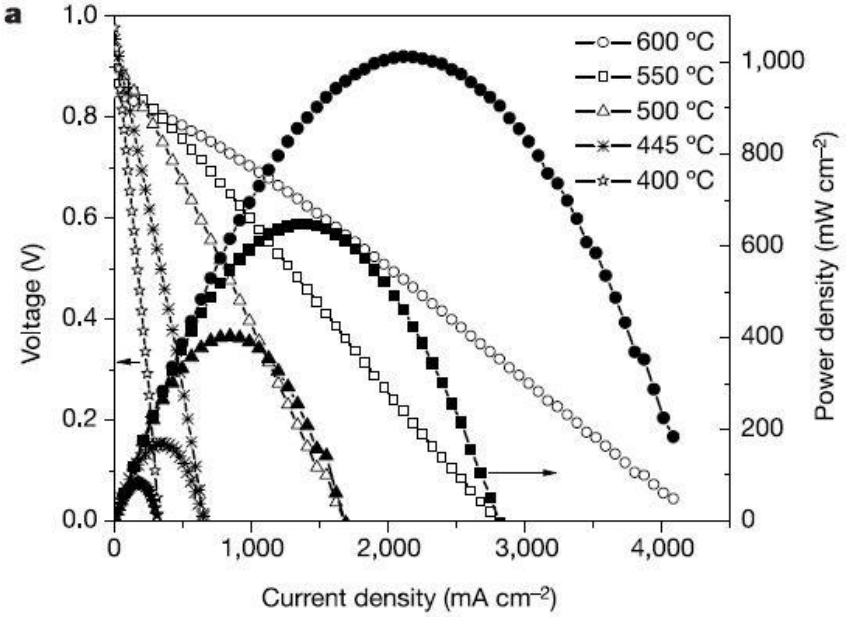

Figure 3.9: BSCF, cell voltage and power density as function of current density at different temperatures in 3% H_2Ohumidified H_2 [45].

4 Experimental

4.1 Synthesis of electrolyte with different dopant concentration

For the sintering of the electrolyte two different methods were used. The first method essentially following the protocol of after the recipe of Babilo et al. [38] was without a wet chemical glycine-nitrate combustion method while the second method comprised a solid state reaction sintering process with added nano powder of NiO as sintering aid. This method was described by Tong et al. [46].

4.1.1 BaZr1-xYxO3-δ sintering without sintering aid

The first attempt to sinter $BaZr_{1-x}Y_xO_{3-\delta}$ was done with a glycine-nitrate combustion synthesis process.

The right ratio of starting materials (Table 4.1) was mixed with glycine, until a molar ration of 1 to 2, glycine to nitrate was obtained. The mixture was dissolved in deionized water until the solution was transparent, then it was heated on a heating plate to 150°C for evaporation to result in a viscous solution. To dehydrate the solution completely it was further heated for several hours in a heating cabinet until a white powder was formed. During this proves caer was token to prevent auto-ignition of the liquid.

The powder was calcined at 1250°C for 5h with a ramp rate of 300°C/h and subsequently ball milled for 1h at 150rpm using isopropanol as a solvent. After drying in a heating cabinet a pellet with a diameter of 25mm was pressed using a binder.

The pellet was then packed in excess $BaZr_{1-x}Y_xO_{3-\delta}$ powder with 10wt% $BaCO_3$ (Figure 4.1) to prevent evaporation of Ba and then sintered at 1600°C with the following ramps: Table 4.1.

Table 4.1: Sintering temperatures and temperature ramps for wet chemical glycine-nitrate combustion synthesis process , where RT is room temperature.

From	To	Ramp rate
RT	1000°C	300°C/h
1000°C	1600°C	60°C/h
1600°C	1600°C	Dwell for 7h
1600°C	RT	300°C/h

Table 4.2: Raw materials used for sintering process

Raw material	Producer	Purity
$Ba(NO_3)_2$	Merck	99.8%
$ZrO(NO_3)_2 * xH_2O$	Alfa Aesar	99.9%
$Y(NO_3)_2 * 6H_2O$	Sigma aldrich	99.9%
NH_2CH_2COOH		

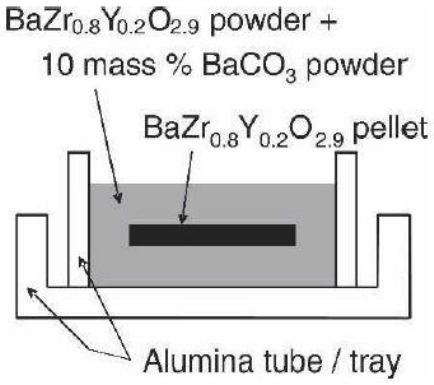

Figure 4.1: Setup for the sintering procedure.

4.1.2 $BaZr_{1-x}Y_xO_{3-\delta}$ with sintering's aid

For the sintering with a sintering aid, a solid-state reactive sintering (SSRS) process was used. To produce the ceramic pellet, the raw materials (Table 4.4) were mixed in the right stoichiometric amounts, dissolved in 2-propanol, then ball milled for 3h at 200rpm and dried in

the heating cabinet for 24h. 2 wt% of NiO was added and mixed with a binder in a mortar before the powder was pressed to a pellet with 25mm diameter.
The pellet was placed on Pt-foil and covered with an alumina cylinder under the sintering process, Table 4.3.

Table 4.3: Sintering temperatures and temperature ramps, SSRS process, where RT is room temperature.

From temperature	To temperature	Ramp rate/ dwell time
RT	800°C	300°C/h
800°C	1400°C	60°C/h
1400°C	1400°C	Dwell for 10h
1400°C	RT	300°C/h

Table 4.4: Raw materials for sintering SSRS process

Raw material	Producer	Purity
$BaCO_3$	Aldrich chemistry	99.98%
ZrO_2	Alfa Aesar	99.7
Y_2O_3	Sigma Aldrich	99.99%
NiO	Sigma Aldrich Nickel(II) oxide, nanopowder	99.8%

4.2 Electrode attachment and fabrication

For the electrode characterisation a half cell was used. In this setup the electrolyte has identical electrodes on both sides and is measured with a two point/four wire setup. For the conductivity measurement of Y-doped barium zirconate platinum electrodes were used. On the electrode part, the electrodes LSM, LSCM, NiO and $La_{0.8}Sr_{0.2}CrO$ were characterized.

Platium paint (Etalor platinum ink 6926) without flux was painted in 3 layers of ca. 10mm diameter on top of each other on the electrolyte. After each layer the paint was dried for 30 min in a heating cabinet at 125°C. In addition a platinum gird of 10mm diameter was cut out, pressed

and painted on top with 2 extra layers of paint. The sample was heat treated at 1100°C with ramp rate of 300°C/h and a dwell time of 2h. After the heat treatment the condition of the electrode was controlled in the SEM.

Inks of pure $La_{0.8}Sr_{0.2}(Mn_{0.5}Cr_{0.5})O_3$ (LSCM) and $La_{0.8}Sr_{0.2}MnO_3$ (LSM), were prepared by mixing the powder with a commercial organic binder (Heraeus V006) and terpinole. The mixing was carried out in at planetary miller at 300rpm for approximately 5 hours.

$LaCrO_3$-paint was provided by Anna Magraso. The painting process is similar to the process described above, with the modification that no platinum grid was used. The sintering temperature and ramp varied for each material and is shown in Table 4.5

Table 4.5: Sintering temperature, ramp rate and dwell time for the electrodes attachment.

Material	Sintering temperature	Ramp rate	Dwell time
	°C	°C/h	h
$La_{0.8}Sr_{0.2}MnO_3$	1100	300	3
$La_{0.8}Sr_{0.2}(Mn_{0.5}Cr_{0.5})O_3$	1100	300	3
$LaCrO_3$	1200, 1350, and 1400°C	300	3

4.3 Scanning electron microscopy

The grain size and chemical inspection of sample was done with a scanning electron microscope (SEM). The chemical composition was investigated by an EDS point analyst, which generates characteristically x-rays when the electron beam interferes with the sample.

4.3.1 Instrument

The instrument used was an FEG-SEM, (Quanta 200F; FEI, USA) in which low and high vacuum conditions can be applied. The two detectors in use are Everhart-Thornley detector

(EDT) and large-field detector (LFD). In addition, a solid-state detector (SSD) for backscatter electrons and Energy-Dispercive detector (EDS) for quantitative analyses were used.

4.3.2 Experimental

The Y-doped barium zirconate samples were polished and washed with 2-propanol before investigation in high, or low vacuum with an acceleration voltage of 10-20kV.

The electrodes were investigated after burning without further treatment in the same conditions.

4.4 Conductivity cell

The conductivity measurements were done in a Probostat cell for (NorECs, Norway) (Figure 4.2). The cell resembles a tube which is closed on the upper side with a sealed inner atmosphere. The sample is mounted inside the cell, with a gas mixer control and thermostat, atmosphere and temperature can be controlled.

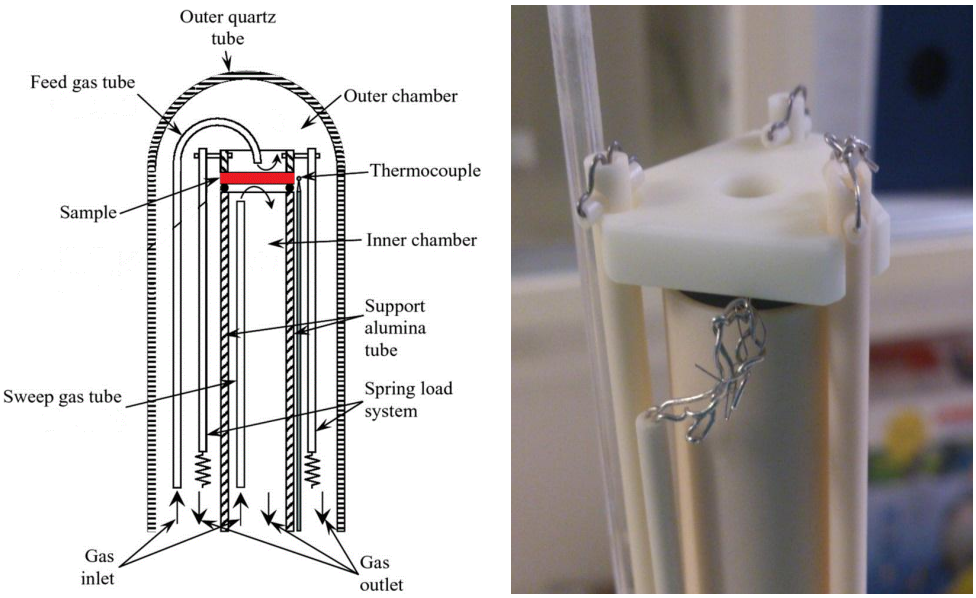

Figure 4.2: Schematic drawing of the Probostat-cell [47] and sample as pellet in original.

The sample is fitted on the top of the carrier tube of alumina. The electrode contact out of platinum was formed as some “fingers” and paced over and under the electrode. On top of the sample is an alumina plate which is spring-loaded and keep the sample on place and in

connection to the electrode contact. The cell has two gas inlets, in order to control to gas atmospheres. In this thesis the same gas was used for both inlets. The sample was not sealed to insure the same gas pressure and atmosphere on both electrodes. The thermocouple was an s-type (Pt+ 10%Rh) and the tube oven configured for that. The bottom part of the cell was cooled to provide overheating.

4.5 Gas mixer

All measurements were done with the same gas mixer (Figure 4.3). The first flow meter could switch between synthetic air or O_2, while the second and fourth flow meter which was dedicated for Ar. The third flow meter determined the flow of mix1. By controlling the O_2 to Ar ratio, a minimal oxygen content of $1* 10^{-5}$atm could be obtained. Wet gas was obtained by leading the gas through H_2O station with saturated with KBr. This insured a constant pH_2O partial pressure of 0.025 atm at 25°C. KBr is chosen because of its partial water pressure is 80% of pure water and that avoid condensation in the copper pipes. For dry conditions the gas is lead through the drying stage which contains P_2O_5. This dry gas still has water contents of 30ppm because of leakage or high flow through. The mixture of dry and wet gasses were used to measure the pH_2O dependency. The last flow meter is dedicated to control the amount of the gas mixture into the cell.

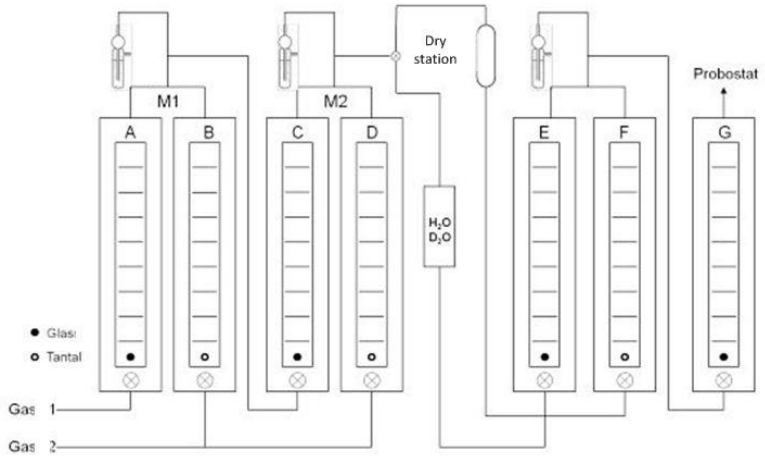

Figure 4.3: Schematic drawing of the gas mixer, where gas 1 is O_2 or Air, and gas 2 is Ar.

4.6 Conductivity measurements

Impedance spectroscopy was done with a standard 2-electrode 4-wire setup. Two different instruments were used for the measurements. The main instrument was a Novocontrol Alpha-A analyser with a 4 wire impedance interface ZG4. The second instrument was a Solatron SI 1260 which a Hewlett Packard 34420A impedance interface. The instruments specifications are shown in Table 4.6.

Table 4.6: Instrument specification

	Alpha-A analyser with ZG4-interface	Solatron SI 1260 with HP34420A interface
Frequency	3μHz-40MHz	10μHz -32MHz
Impedance	10^{-4}-10^{14}Ω	10^{-4}- 10^{13}Ω
AC signal out	100μV-3V	100μV-9.5V
Software	WinDETA	Omega
Error accuracy	0.003%	0.1%

4.6.1 Experimental

The electrolyte impedance spectroscopy measurements were done in a frequency range from 1MHz to 1Hz with an acceleration voltage of 0.1V. For the electrode study a frequency range from 1MHz down to $1*10^{-3}$Hz and acceleration voltage of 0.05V was chosen.

4.7 Software

The impedance data were deconvoluted with EqC [48], which enabled the estimation of parameters to analyze the electrolyte and electrode performance.

With usage of the EqC-software, it was possible to fit measured results to a chosen equivalent circuit. It was possible to monitoring and control the error by estimating the mismatch of the actual data and the fitted results. Because some resistances can be considerably larger than in others cases it could not be excluded that the smaller resistances were unaffected (more than 1 order of magnitude differences). However, because EqC was not designed to provide exact

values, but rahter estimates of resistances, small errors can be accepted as they will not affect the overall characterization of the processes at the electrolyte and electrode.

5 Results

5.1 Electrolyte

Figure 5.1 shows the grain size of the electrolyte for $BaZr_{0.8}Y_{0.2}O_{3-\delta}$, $BaZr_{0.85}Y_{0.15}O_{3-\delta}$, and $BaZr_{0.9}Y_{0.1}O_{3-\delta}$. In each of the samples the grains are evenly distributed. BYZ20 and BYZ10 were sintered at 1600°C with the same amount of 2wt% nano NiO as a sintering aid. It is clearly visible, that BYZ20 has small grains in the range of 1-2µm, while the 10% yttrium doped sample has bigger grains with a size between 2-4µm. The SSD detector displays a homogeneous surface without secondary faces.

The grains in the BYZ15 sample are somehow different with grains in the range of 2-4µm, but boundaries that are not so sharply defined. It appears that the grains coalesced and that crystals are much more rounded than those of the BYZ20 and BYZ10 samples.

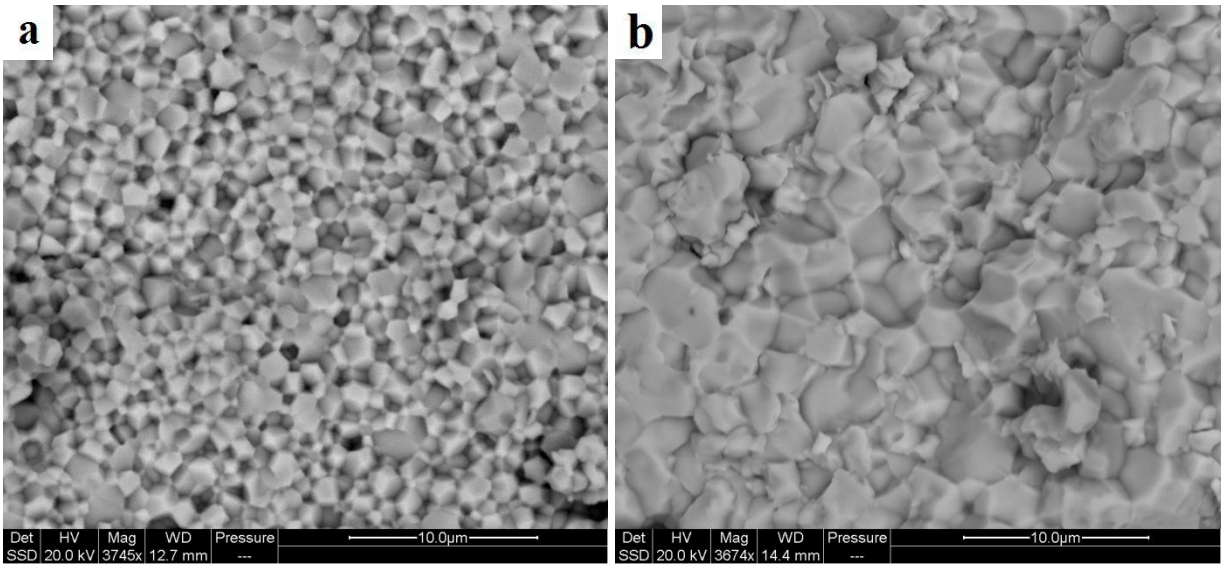

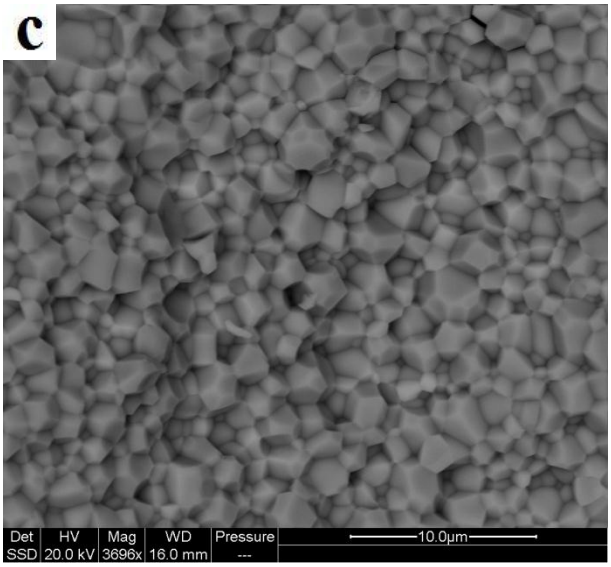

Figure 5.1: BYZ20 (a), BYZ15 (b) and BYZ10 (c). SEM-analyses are done in high vacuum, with an acceleration voltage of 20kV. The figures display the image of the SSD detector.

The chemical composition was determined with EDS-analyses. Some of the signals, especially those for zirconium and yttrium were overlapping. As a results, the analyses have an error estimate of 2-3 at%. However, because this analyse was used to indicate the right ratio between the elements, this rate can be neglected. The following tables showing state the estimated values for at% and the measured at%.

Table 5.1: EDS-analyze of BYZ20 under high vacuum with an acceleration voltage of 20kV

Element	EDS-analyse [at%]	Theoretic [at%]
Ba	49.0	50
Zr	42.7	40
Y	8.3	10

Table 5.2: EDS-analyze of BYZ15 under high vacuum with an acceleration voltage of 20kV

Element	EDS-analyse [at%]	Theoretic [at%]
Ba	48.1	50
Zr	42.7	42.5
Y	7.1	7.5

Table 5.3: EDS-analyze of BYZ10 under high vacuum with an acceleration voltage of 20kV. Analyse included at% of Ni and O, therefore are different numbers displayed.

Element	EDS-analyse [at%]	Theoretic [at%]
Ba	29.70	33
Zr	28.12	29.7
Y	3.2	3.3

5.2 Interpretation of Impedance spectra

A temperature interval of 150-600°C was used to characterise the electrical properties of the electrolyte. The frequency range from 1MHz to 1Hz was used to observe the different contributions of bulk interior and grain boundary to the electrolyte. The samples were prepared as described in section 4.1.2. For the evaluation of the Nyquist diagram, 3 different models were used. All measurements were done in wet atmosphere in air, and were corrected for the geometry.

5.2.1 Temperature dependency of $BaZr_{0.8}Y_{0.2}O_{3-\delta}$

In the temperature range of 150-300°C both the bulk and grain boundary contribution were recorded ant the values could be fitted as an (RQ) circuit. The electrode was not seen at this low temperature, resulting in equivalent circuit $(R_1Q_1)(R_2Q_2)$, (in this chapter 1 and 2 stands for the bulk and grain boundary, respectively). In the temperature range of 400-600°C the bulk interior was suppressed by the grain boundary and lies only as one resistor in front of the grain boundary semicircle. The electrode resistance increased resulting in a $R_1(R_2Q_2)(R_3Q_3)$ circuit, (3 denotes the electrode part). At high temperatures above 500°C an increasing induction was observed. For this fitting the $LR_1(R_2Q_2)(R_3Q_3)$ circuit was used.

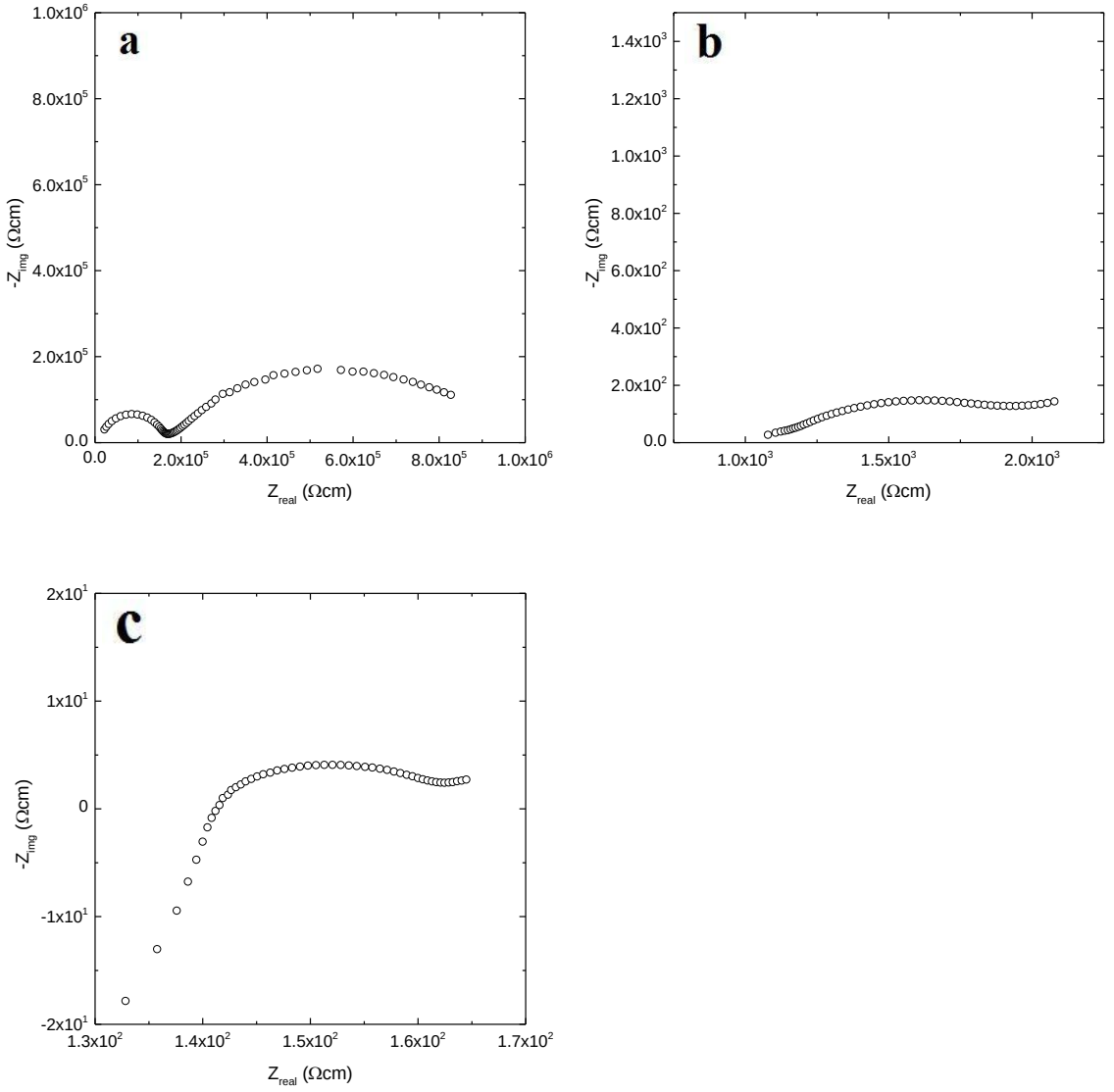

Figure 5.2: Impedance sweeps at 150 (a), 400 (b) and 600°C(c), in wet air conditions.

The following conductivity plot of bulk, grain boundary, specific grain boundary and total conductivity was achieved by deconvolution of the impedance data with EqC. The raw data for the EqC fitting can be seen in appendix A, (Table 9.1).

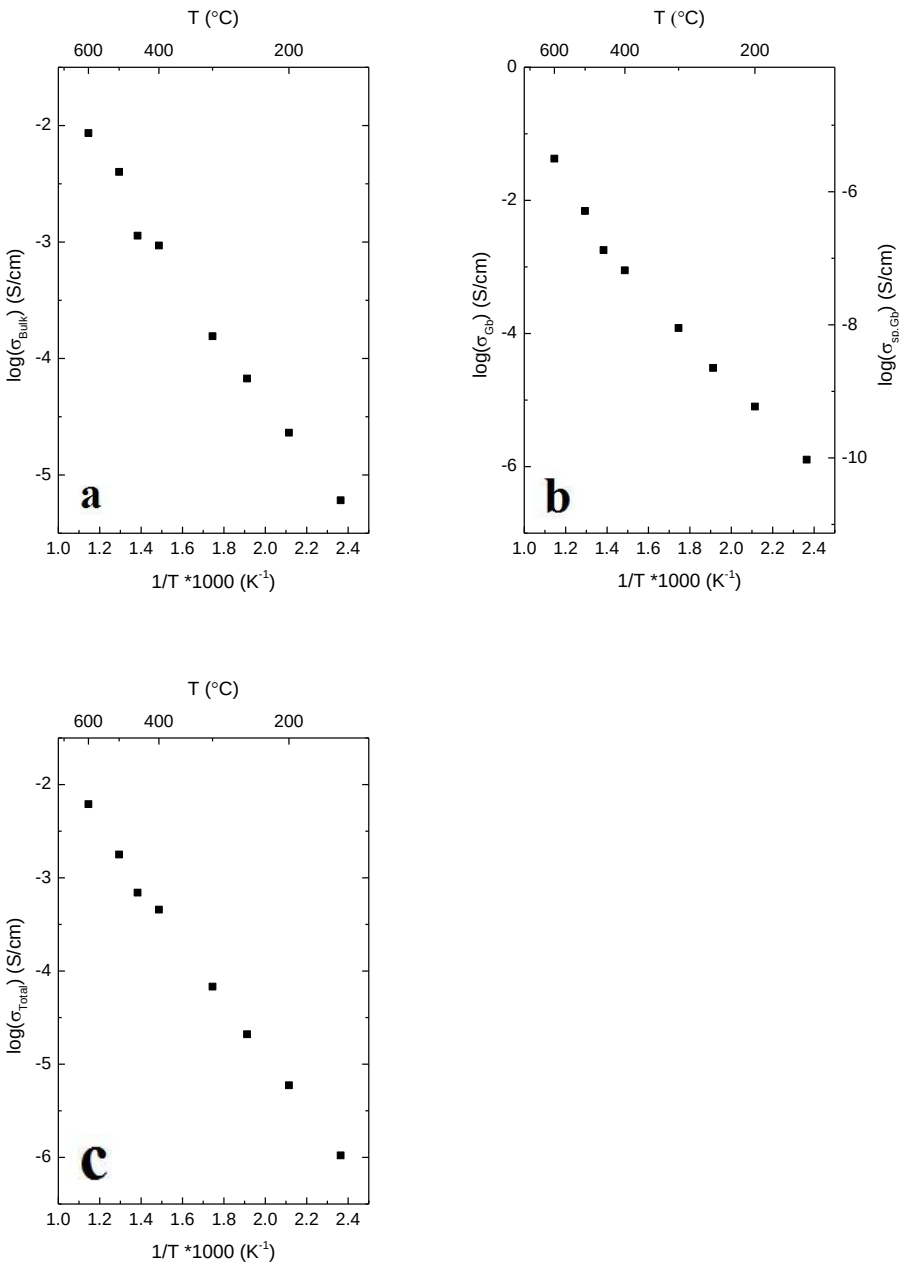

Figure 5.3: Arrhenius plot of $BaZr_{0.8}Y_{0.2}O_{3-\delta}$ for bulk (a), grain boundary (b) and total conductivity(c) in wet air atmosphere for BYZ20.

5.2.2 Temperature dependency of $BaZr_{0.85}Y_{0.15}O_{3-\delta}$

For this sample the same equivalent circuits were used as mentioned above, with the exception for the 500 and 600°C measurement where it was not necessary to use an inductor in front of the circuit.

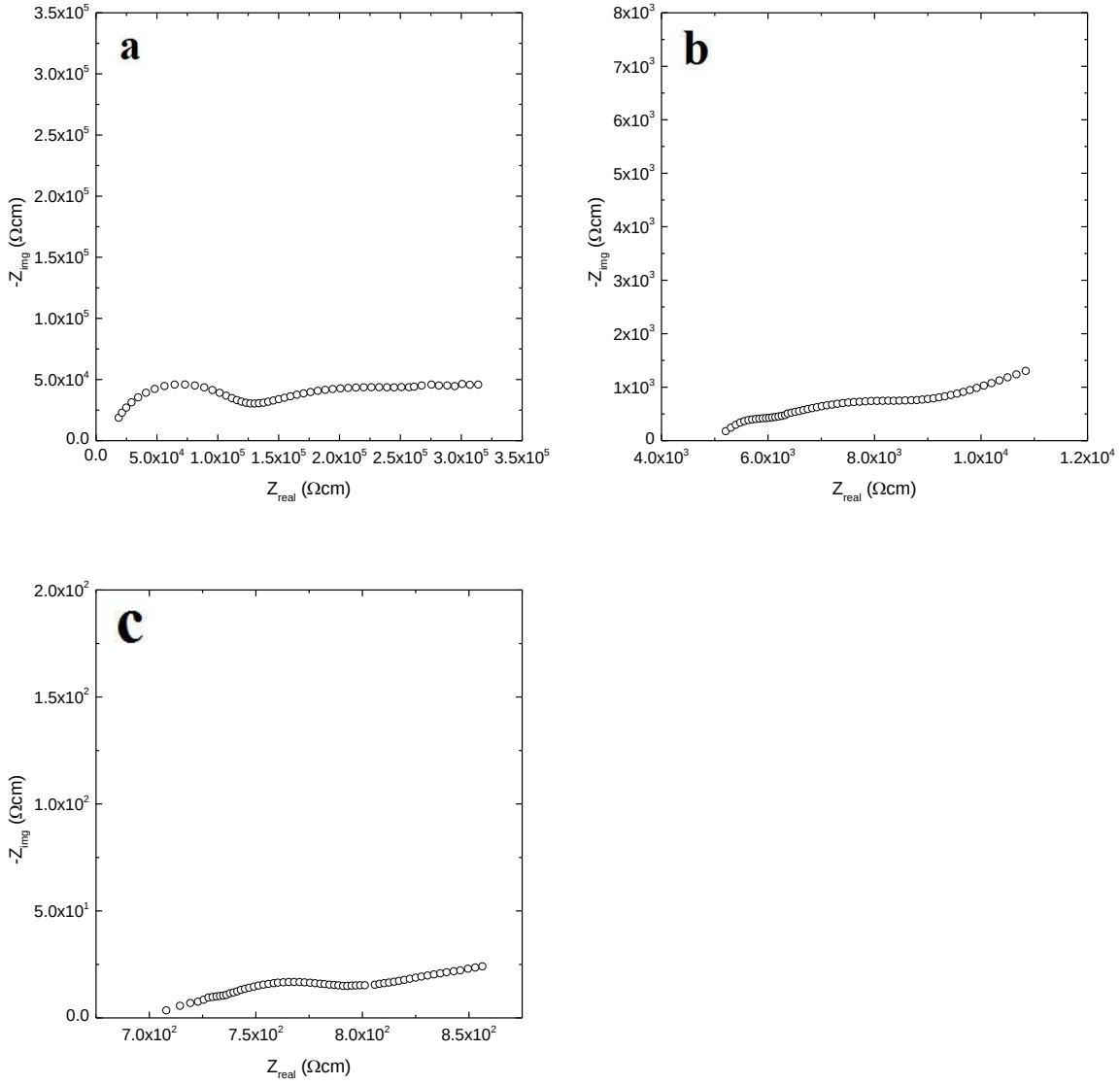

Figure 5.4: Impedance sweeps at 200(a), 400(b) , and 600°C (c) in wet air for BYZ15.

The following Arrhenius plots shows the conductivity results achieved by the deconvoluting of the sweeps. The outcome of the fitting can be seen in Table 9.2, in appendix A.

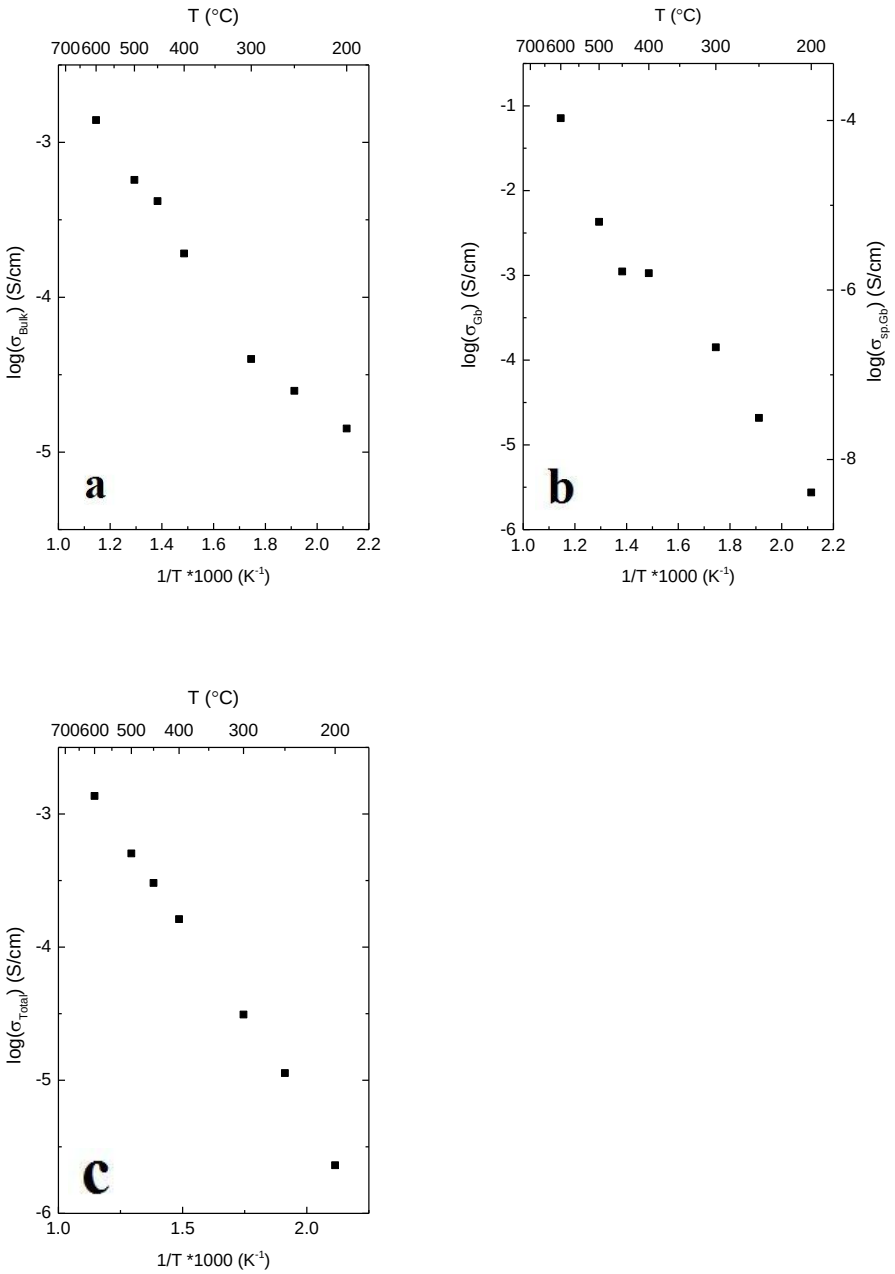

Figure 5.5: Arrhenius plot of $BaZr_{0.85}Y_{0.15}O_{3-\delta}$ for bulk- (a), grain boundary-(b) and total conductivity (c) measured in wet air.

5.2.3 Temperature dependency of $BaZr_{0.9}Y_{0.1}O_{3-\delta}$

For the 10% doped sample a slightly different model was used. At the temperatures of 150 and 250°C the equivalent circuit $(R_1Q_1)(R_2Q_2)$ resulted in the best fit. From 250°C to 550°C the bulk was no longer seen, therefore (R_1Q_1) was replaced with resistance R_1, and the equivalent circuit

obtained was $R_1(R_2Q_2)(R_3Q_3)$, where (R_3Q_3) stands for the electrode. At the highest temperature (650°C) an inductance (L-element) was used in front of the equivalent circuit.

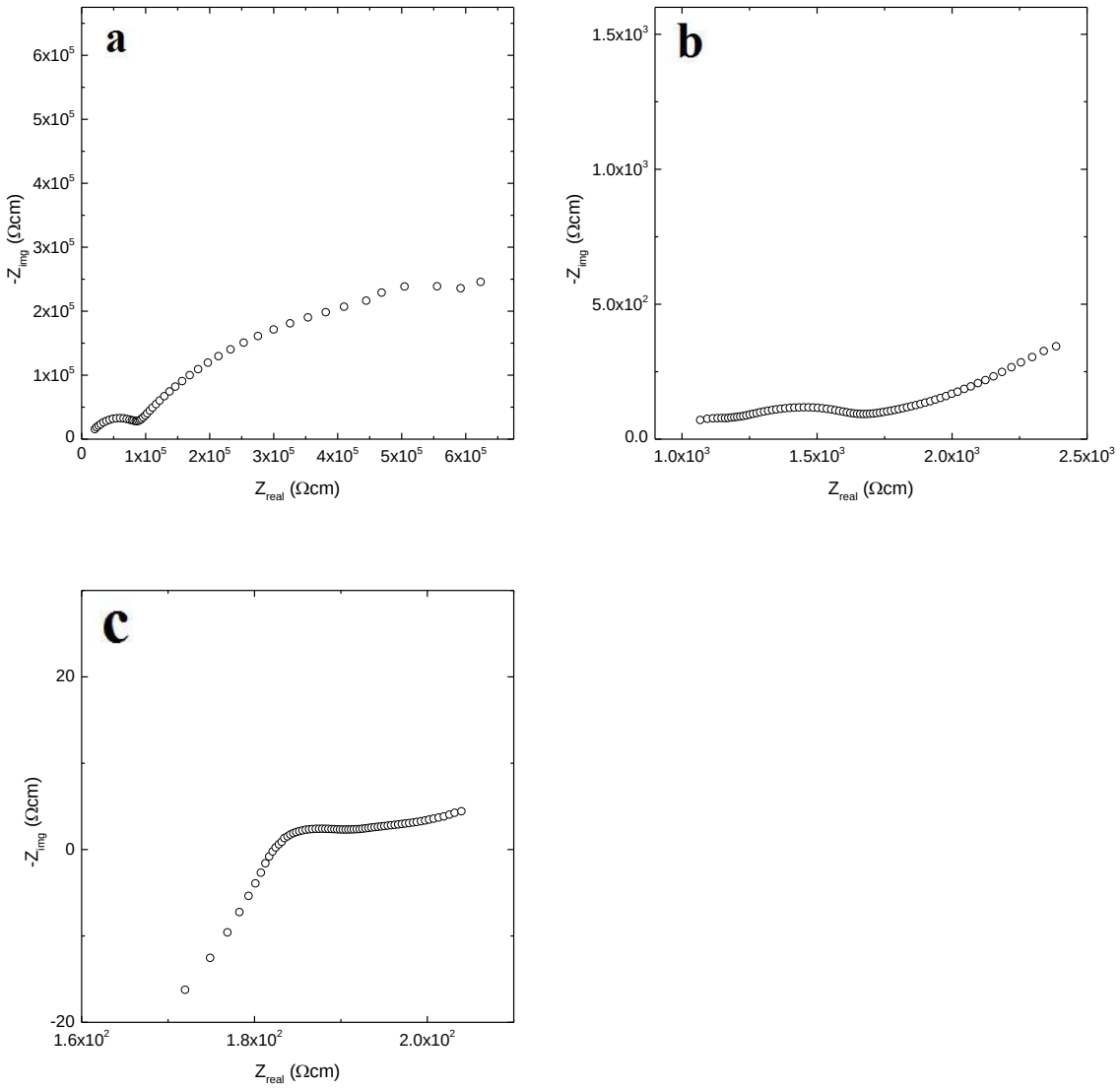

Figure 5.6:Sweeps at temperature of 150 (a), 450 (b) and 650 (c)°C form 10 MHz to 1HZ done in wet air.

The following plots are the conductivity of bulk, grain boundary, specific grain boundary and total conductivity of the BYZ10 sample in wet air. The outcome of the fitting can be seen in Table 9.3, appendix A.

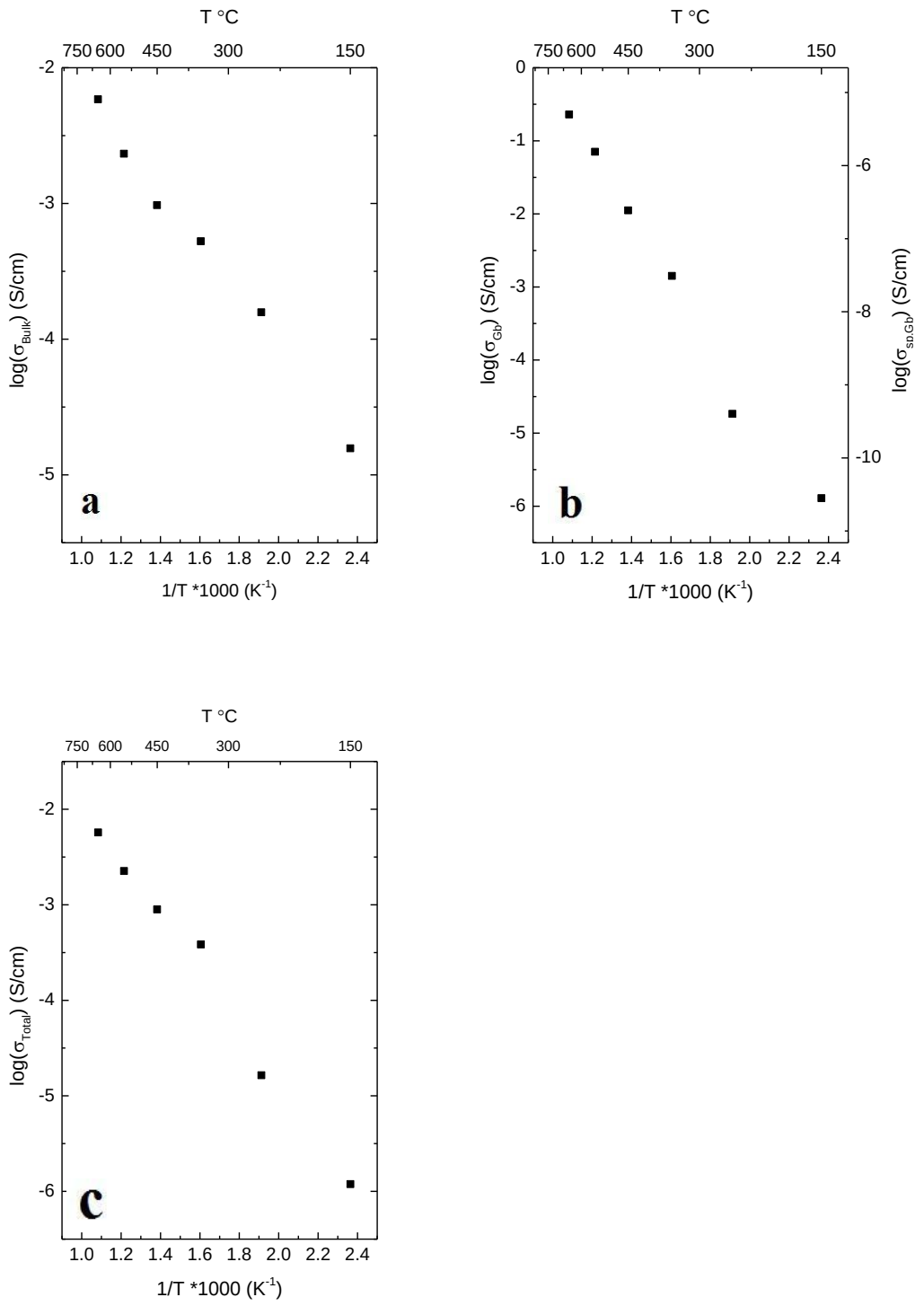

Figure 5.7: Arrhenius plot of $BaZr_{0.9}Y_{0.1}O_{3-\delta}$ for bulk (a)-, grain boundary (b)-, and total (c) conductivity measured in wet air.

5.2.4 Oxygen dependency of $BaZr_{0.9}Y_{0.1}O_{3-\delta}$

The measurements of the oxygen partial pressure dependencies for $BaZr_{0.9}Y_{0.1}O_{3-\delta}$ were done in wet conditions at 450°C. The first measurement point was in pure argon with an oxygen content of $1*10^{-5}$ atm. Oxygen was then introduced for the next measurement point. After equilibrium was reached the impedance sweep was done. This procedure was repeated for different oxygen partial pressures, until pure oxygen was reached.

Figure 5.8 shows that the pO_2-dependency had the biggest influence on low frequency semi-circle, which is assigned to the polarisation resistance of the electrode. The grain boundary resistance shows only slight effects. The conductivity simultaneously decreased with falling pO_2. The bulk conductivity remained unaffected at a temperature of 450°C. When considering the total electrolyte as conductivity, a significant oxygen dependency was not obvious (Figure 5.9).

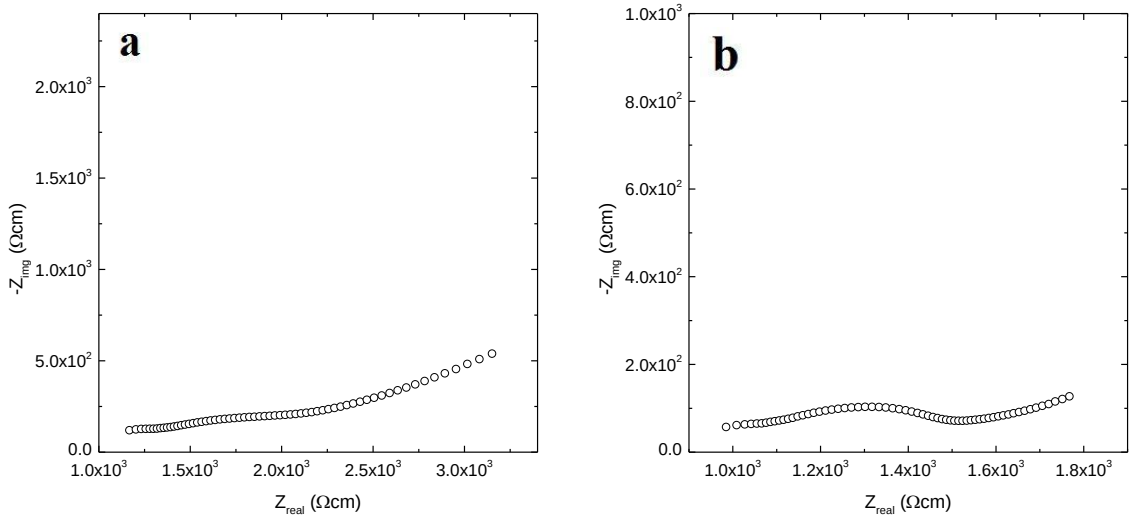

Figure 5.8: Nyquist plot for pure wet Ar (a) and and pure wet O_2 (b)

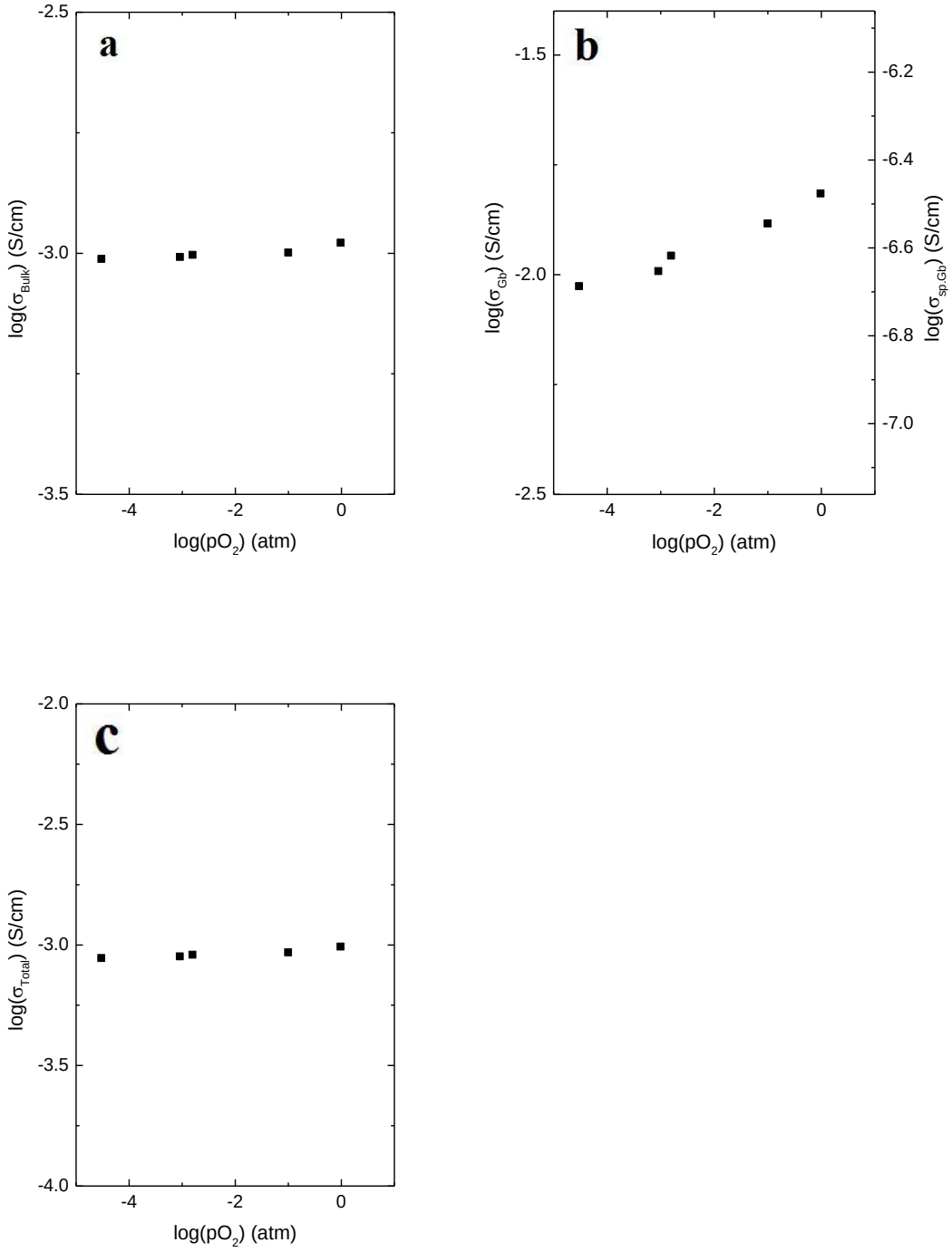

Figure 5.9: The bulk conductivity, with an slope of 0.006 (a), the grain boundary conductivity with an slope of 0.047 (b) and the total conductivity with an oxygen partial dependency of 0.01 (c).

5.2.5 Water vapour pressure dependency of $BaZr_{0.9}Y_{0.1}O_{3-\delta}$

Within the range of the water vapour pressure, conductivity was measured in air at 600°C. The first impedance sweep was done in dry conditions and subsequently with H_2O stepwise increasing. Due high inductance and noisiness of the sweeps the equivalent circuit R_T(RQ) was used, where the R_T stands for the total resistance of the electrolyte (this could not be separated to the bulk and grain boundary). The (RQ) element was associated to the electrode, more specifically to the charge transfer resistance.

The plot shows an increase of conductivity with increasing partial pressure of water. The differences are a half order of magnitude. The slope shows a pH_2O dependency of -0.27.

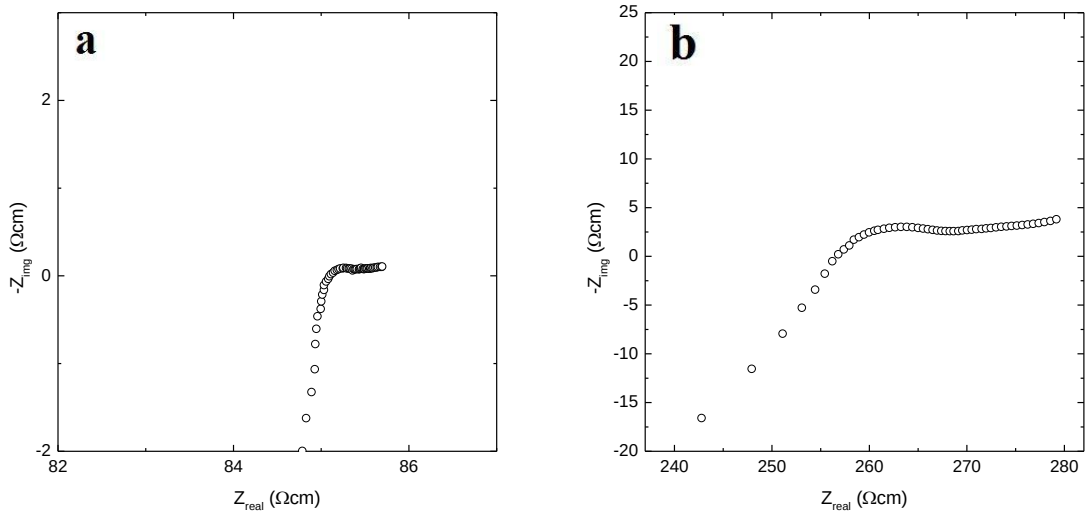

Figure 5.10: Impedance sweep for dry conditions (a) and wet conditions (b) in air.

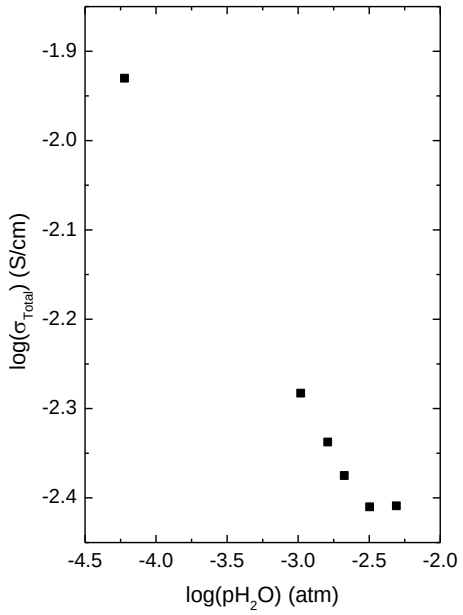

Figure 5.11: Total conductivity of the electrolyte, with a pH_2O dependency of -0.27 in air.

5.2.6 Comparison of 20%, 15%, and 10% Y-doping

For better comparison, BYZ20, BYZ15 and BYZ10 were plotted together in one graph to demonstrate conductivity. Figure 5.12 shows the total-, bulk-, grain boundary, and specific-conductivity.

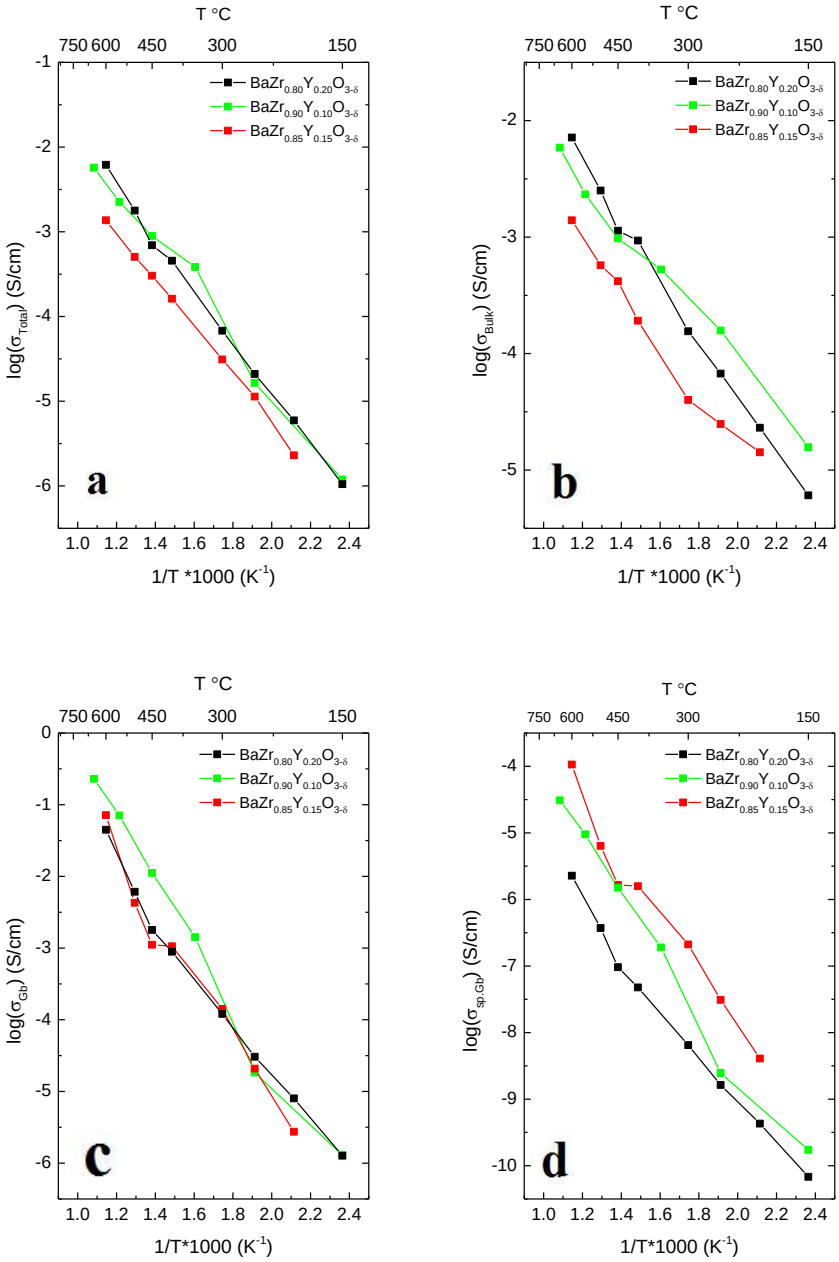

Figure 5.12: Total-(a), bulk–(b), grain boundary-(c), and specific grain boundary-(d) conductivity, were black represent BYZ20, red BYZ15, and green BYZ10. The measurements were done in wet air atmosphere.

For further comprising the Schottky height was calculated by formula (2.15). The resulting values are represented in the following figure.

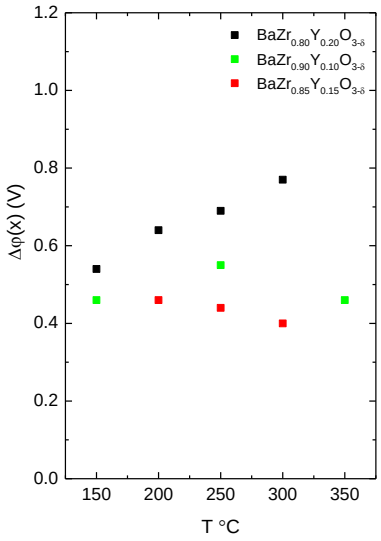

Figure 5.13: Schottky high for BYZ20 (black), BYZ15 (red), and BYZ10 (green), calculated from the conductivity measurements is wet air.

5.3 Microstructure and electrode-electrolyte interface

The electrode morphology was examined with SEM before and after the electrical characterization. In particular, the interface between the electrode and the electrolyte was analysed after sintering and impedance measurement. This was to further our understanding of the electrode performance. For samples which were not electrically characterized, cross sections can provide an indication of the compatibility between electrolyte and electrode.

5.3.1 Electrode morphology of $LaSrMnO_3$

The LSM-electrode hand painted on the $BaZr_{0.8}Y_{0.2}O_{3-\delta}$ (BYZ20) pellet. Figure 5.14 shows the pure BYZ20 (upper left), the reacted phase (light stripe in the central picture) and the pure LSM at the lower right.

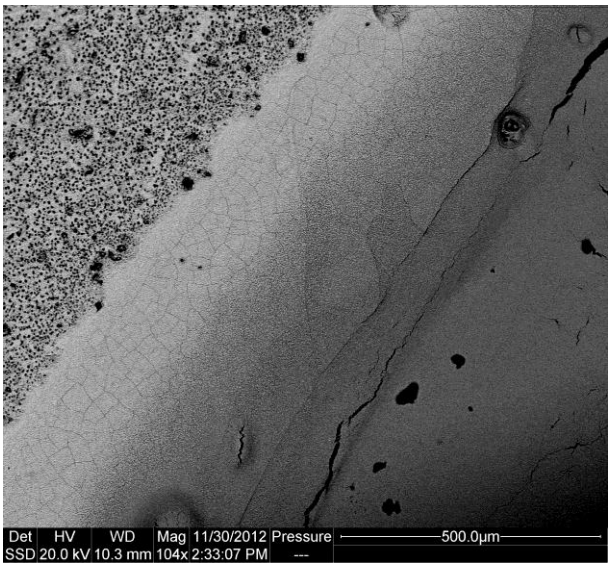

Figure 5.14: LSM electrode on BYZ20 done in high vacuum, SSD image in high vacuum with acceleration voltage of 20kV.

5.3.2 Electrode morphology of $La_{0.75}Sr_{0.25}Cr_{0.5}Mn_{0.5}O_{3-\delta}$

Figure 5.15a visualizes the boundary between the painted electrode and electrolyte. The borderline is sharp and readily identifiable. The electrode and electrolyte are closely spaced, indicating that no chemical reaction occurred and that both are compatible. The grains size of the electrode is smaller than 1µm, and the electrode surface appears to be porous for better gas diffusion. Figure 5.15 b pictures the LSCM-electrode after the electrochemical measurements.

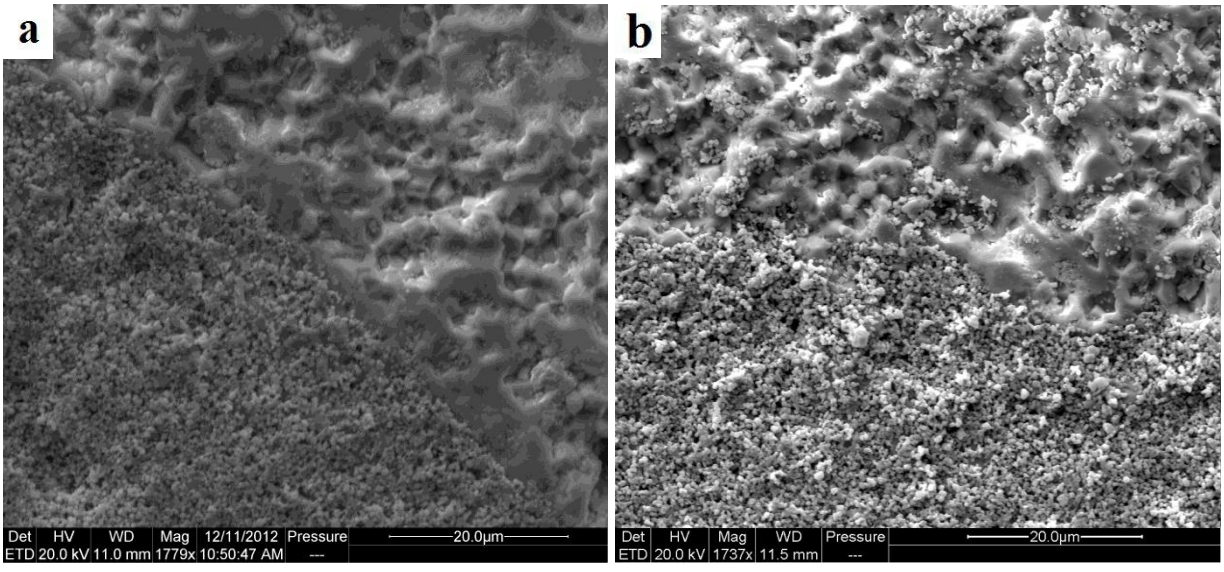

Figure 5.15: $La_{0.75}Sr_{0.25}Cr_{0.5}Mn_{0.5}O_{3-\delta}$ painted on BYZ20 a) To the upper right shows the BYZ-electrolyte and the downer left the pores LSCM-electrode with 1µm grain size. b) After electrical-measurement , ETD image in high vacuum with acceleration voltage of 20kV.

5.3.3 $LaCrO_3$

Figure 5.16a shows the cubic $LaCrO_3$-crystals overlying the BYZ20 electrolyte. The grains have a size of less than 2.5µm and are evenly distributed. The boundary between the electrolyte and electrode is distinct and there is no sign of reaction. The cracking of the electrode is pictured in Figure 5.16b. The electrode structure curls and rolls up and subsequently the electrode is destroyed. In Figure 5.16b the darker material is the electrode, while the brighter material is the BYZ20. The thickness of the electrode which can be observed form the rolled material can provide an indication about the behaviour of the electrode. A thinner electrode may be more resistant against cracking and pealing.

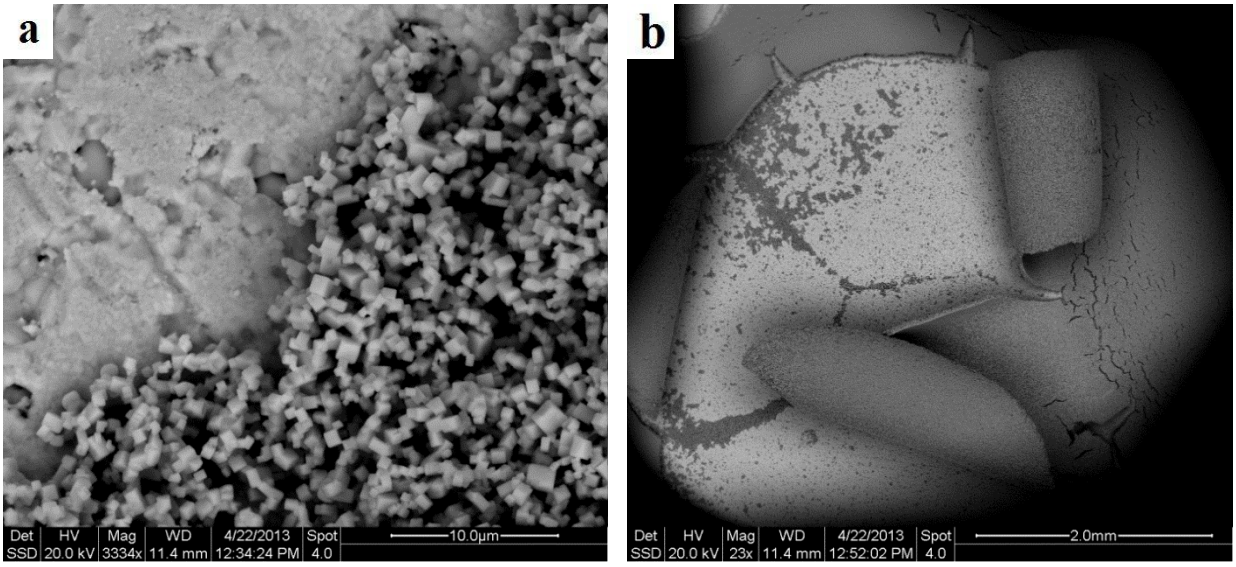

Figure 5.16: a) shows the interface between electrolyte (left) and LaCrO3 right. b) shows the electrode (darker) pealing of from the electrolyte (lighter), ETD image in high vacuum with acceleration voltage of 20kV.

5.4 Cross section of electrodes

The cross section analyse was done by SEM. The LSM sample was broken in the middle after the observation of the secondary phase as described in section 5.3.1. The cross section of LSCM sample was investigated in SEM after the electrical-characterisation. The sample was prepared similarly to that of LSM.

5.4.1 LSM-cross section

Figure 5.17 shows the LSM|BYZ20 interface. The electrode has an even morphology. The LSM is well connected to the electrolyte and has an open and porous structure which insures the gas-exchange. Due to the small particle size of the electrode the three phase boundary becomes longer. The secondary phase as shown in Figure 5.14 could not be observed in the cross sections. The electrode is approximately 25µm thick.

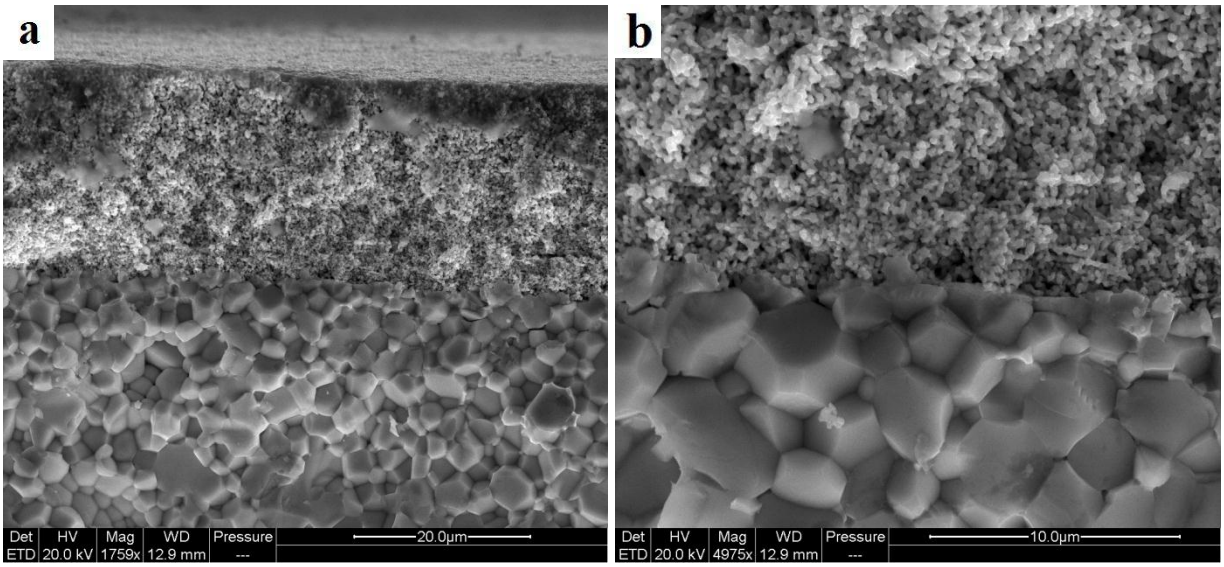

Figure 5.17: Cross section of LSM, where the upper part is the electrode and in the bottom the electrolyte, ETD image in high vacuum with acceleration voltage of 20kV.

5.4.2 LSCM

The images (Figure 5.18) shows the morphology. The LSCM|BYZ20 interface is clear with the electrode as a second layer on the electrolyte. The LSCM electrode appears to be more dens than the LSM electrode. It is difficult to evaluate degradation of the electrode, but the contact between electrode electrolyte is still realized given. The Electrode is approximate 10µm thick.

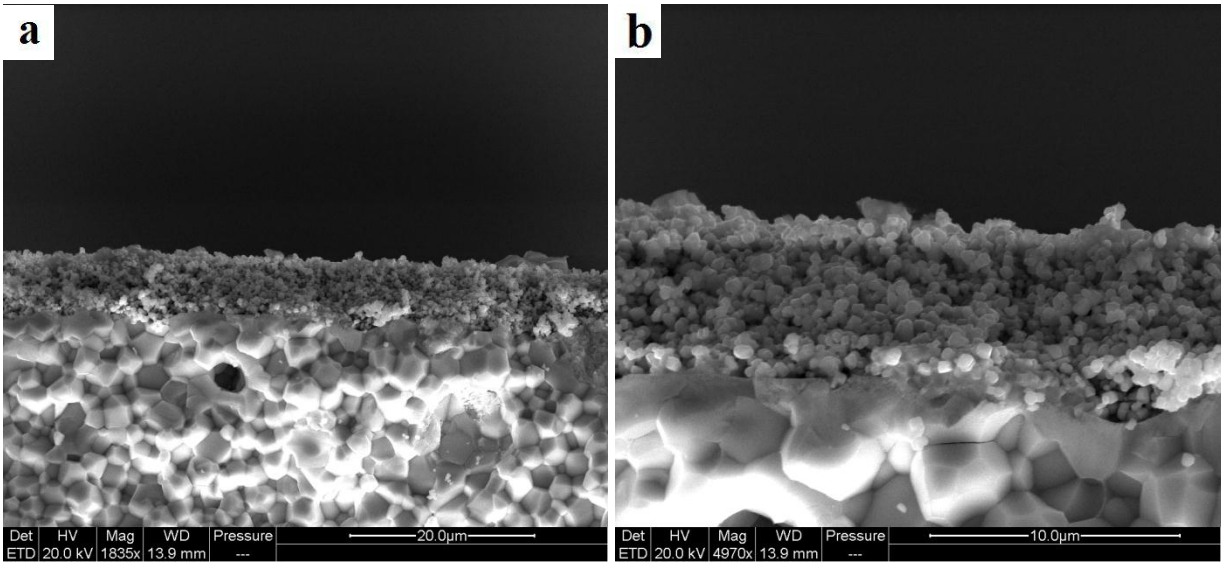

Figure 5.18: LSCM cross section, where the upper part is the electrode and in the bottom the electrolyte, ETD image in high vacuum with acceleration voltage of 20kV.

5.5 Interpretation of electrodes impedance spectra

The different processes at the electrode were measured by impedance spectroscopy. The results of temperature, pO_2 and pH_2O measurements can provide indications for the processes and identify which electrode process are rate limiting.

5.5.1 Temperature dependency

The experimental aspect is to investigate the electrode, bulk and grain boundary were constrained to constitute only one resistance in series with the electrode. For the electrode circuit a modified Randel circuit was used, section (2.4.1). It has a capacitor in parallel to a resistor (R_{mf}) and a Gerischer dispersion (G). The different responses of these two elements were correlated with charge transfer (CT) and diffusion resistance, respectively. Its validity will be discussed later. However the total resistance of the electrode is composed of the middle frequency part (mf), and low frequency part (lf).

The circuit described above was used for a temperature interval between 500 and 650°C. Because the Gerischer dispersion does not permit to calculate the capacitance, the low frequency range was fitted to an ordinary (RQ)-element. By this modification the original Randle circuit as

described in section (2.4.1) was obtained. This modification was necessary for a rough estimate of the capacitance at low frequency. The temperature deviation in the upper range created an increase in noise and inductance, thus making the impedance sweeps difficult to interpret. Finally the simple R(RQ)-circuit was used for the best reasonable fits.

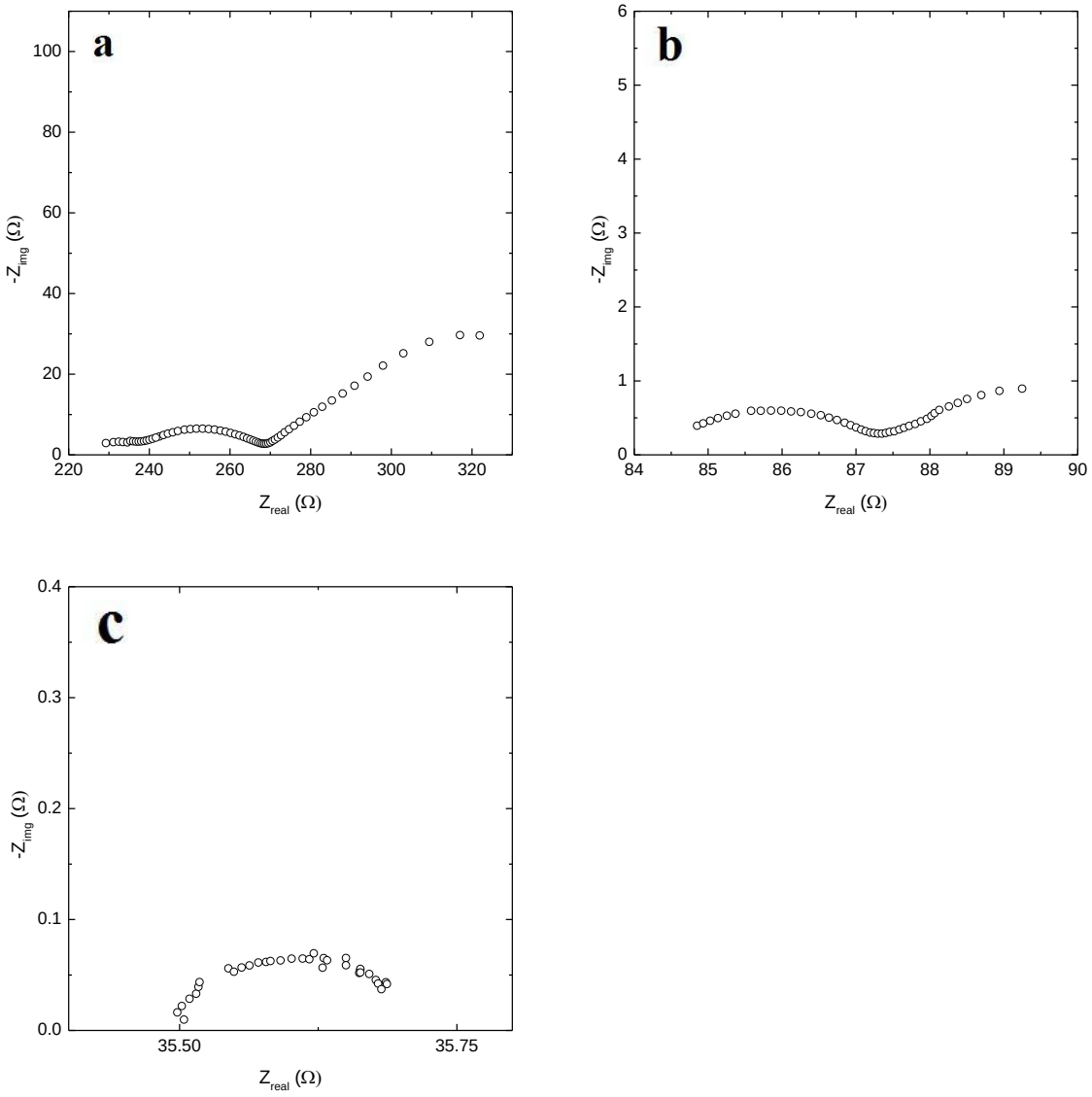

Figure 5.19: Impedance sweep at 500, 650 and 800°C, respectively. Measurements were done form 1MHz to $1*10^{-3}$Hz in wet air. The Bulk and Grain boundary contribution was removed.

The capacitance of the medium frequency semi-circle was calculated according to the pseudo capacitance (see equation (2.23)). At the temperature range between 500 and 650°C the

resistance for the Gerischer disruption was calculated using the equation (2.26). Due the (RQ) fitting it was possible to calculate the pseudo capacity by equation (2.23).

At temperatures above 700°C, the charge transfer and Gerischer impedance overlapped and this overlapping resistance prevented a fully isolated investigation of the two semi-circles. This resistance consisted of both the middle range polarization resistance and low frequency polarisation resistance.

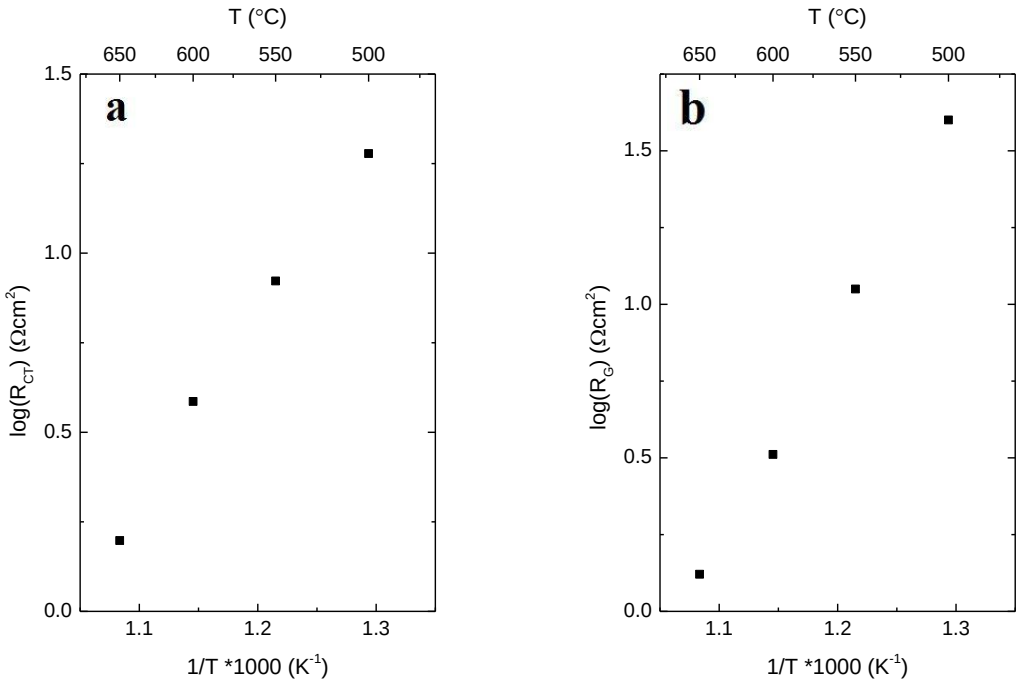

Figure 5.20: Temperature dependencies of polarisation resistance of middle (a) and low (b) frequency arcs in wet air.

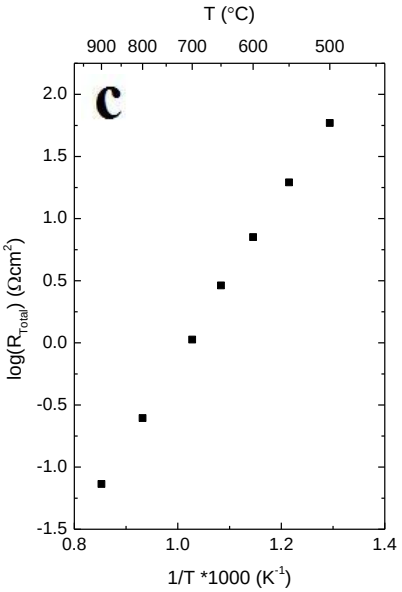

Figure 5.21: The total polarization resistance of the electrode. Log R vs. 1/T

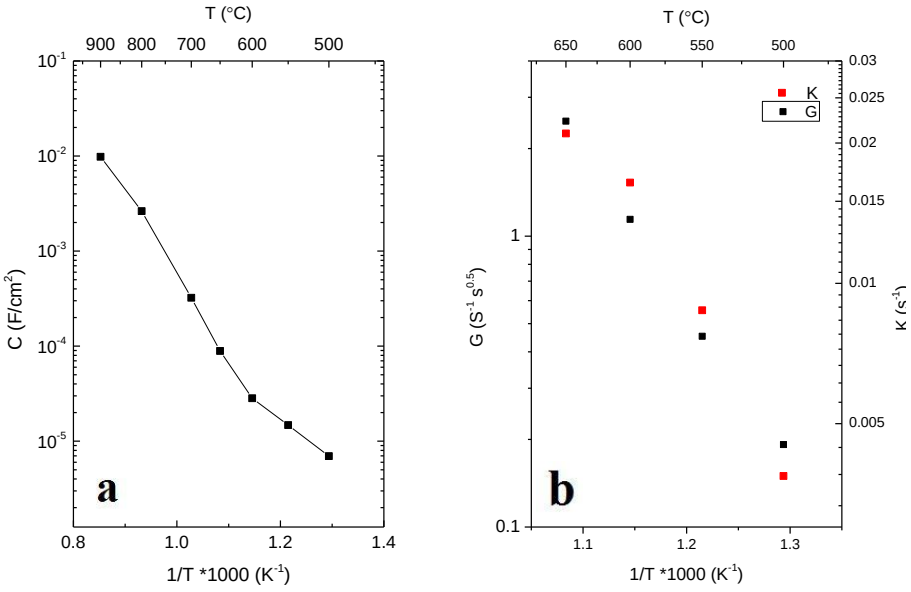

Figure 5.22: The charge transfer pseudo capacitance (a), and parameters K and G values for the Gerischer (b) measurements was done in wet air.

5.5.2 Oxygen dependency

The oxygen partial pressure measurement was done in wet conditions at a temperature of 650°C. Figure 5.23 shows the different impedance spectra, each measured at a different oxygen partial pressure.

The oxygen partial pressure appeared to have an effect on electrolyte, and electrode processes. In case of the electrolyte, the assumption of one resistance for the bulk and grain boundary was still valid. With decreasing the oxygen content an increase of resistance was is observed (pO_2 dependency of 0.056). Correspondingly, the lowest oxygen concentrations resulted in the highest resistance for the diffusion process at the electrode. However, for the lowest oxygen containers the diffusion process had the biggest resistance, which changed at an oxygen pressure of ca. $5*10^{-2}$ atm when the charge transfer was most resistive. In summary, the oxygen pressure effects on the polarization resistance of electrode and the electrolyte and reaches highest resistance with decreasing oxygen pressure.

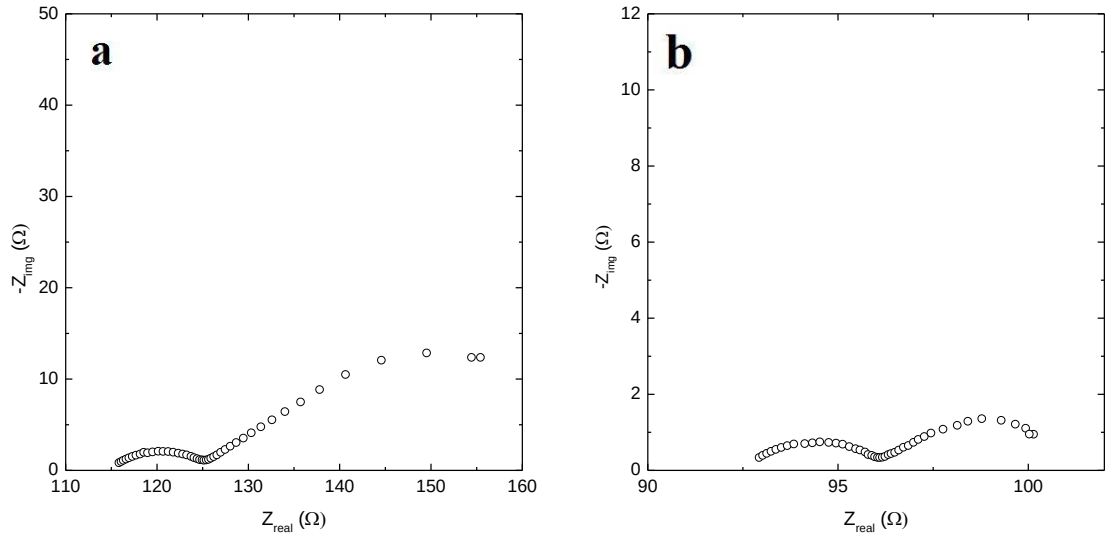

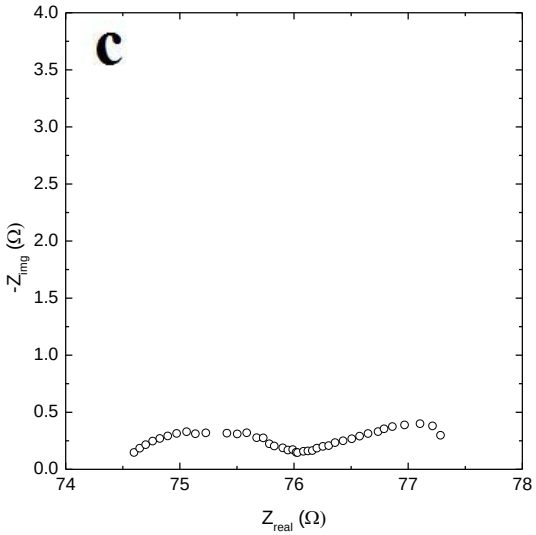

Figure 5.23: Impedance sweep depending on oxygen partial pressure, done at 650°C in wet conditions for Ar (a), pO_2 5*10-2 (b) and O_2 (c).

Figure 5.24 illustrates the different effects of the resistance within the electrode, proving the electrodes dependence on the oxygen partial pressure. The plots show decreasing values by decreasing with the oxygen content.

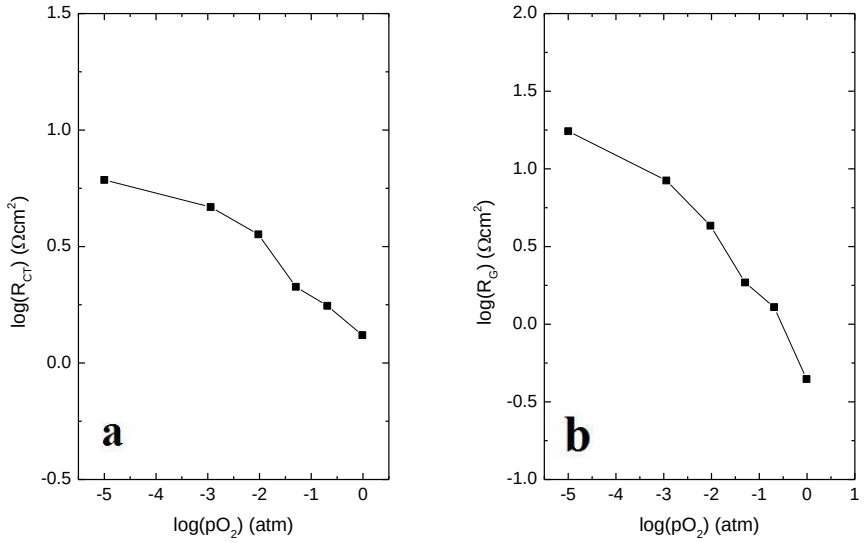

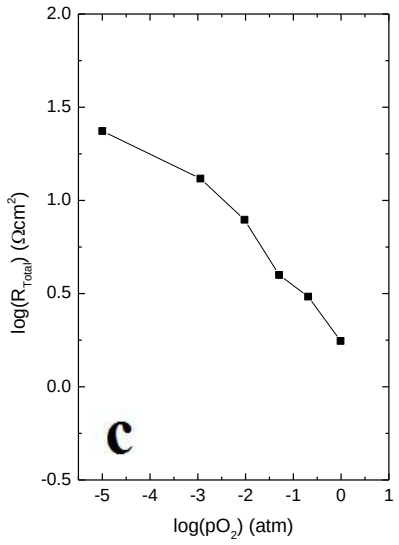

Figure 5.24: log(pO_2)vs. log(R) of the R_{mf} (a), and R_{lf} (b) and total polarization resistance (c) measured at 650°C in wet conditions.

5.5.3 Water vapour dependency

The atmosphere humidity was gradually increased from 6*10^{-5}atm to 0.026 atm at 650°C in order to investigate the pH_2O dependency of R_{mf} and R_{lf}. To avoid noise a R(RQ) circuit was used for the convolution, shown in Figure 5.25. It was not possible to distinguish between the R_{mf} and R_{lf} as done in the sections above. Because bulk and the grain boundary could not be differentiated, they were unified as one resistor in front of the electrode. The conductivity plot shows none water vapour dependency (Figure 5.26). The electrode was fitted to the (RQ). As only few points in the sweeps could be used, and because there was interference from a high degree of noise, the results obtained should be treated with caution. The water vapour dependency is measured to be 0.17.

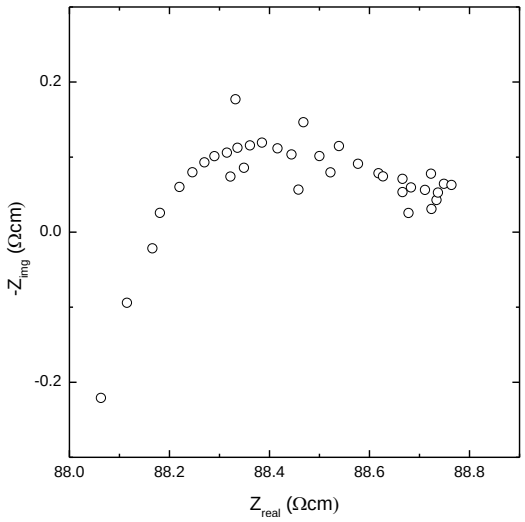

Figure 5.25: Illustration of the noise in the sweep

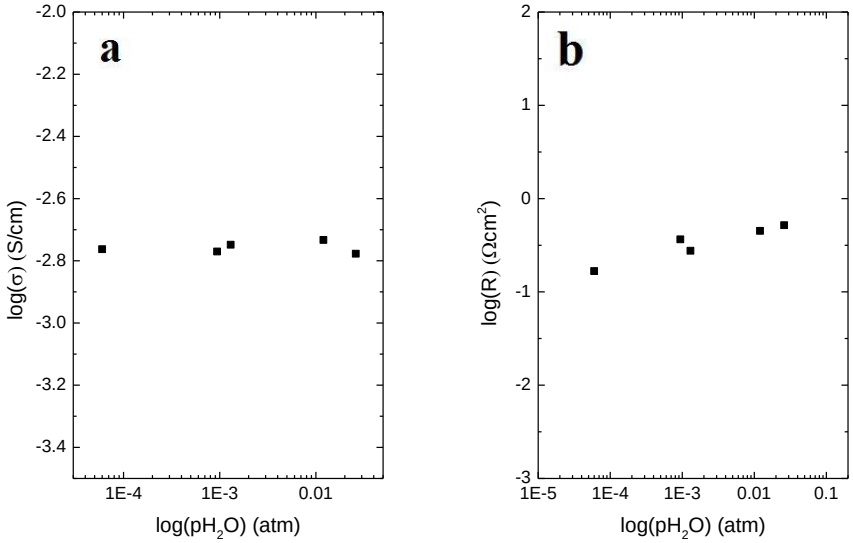

Figure 5.26: logarithmic conductivity of Bulk and grain boundary (a) and total polarization resistance (pH_2O-dependency of 0.17) (b) as function of pH_2O

Table 5.4: Activation energies for the low frequency arc, middle frequency arc and total polarization resistance

Semi-circle	Activation energy	
	eV	kJ/mol
mf	0.94	90.41
lf	1.34	129.18
Total	1.24	119.31

6 Discussion

6.1 Density

It is well known that barium zirconate based ceramics are hard to sinter. Without sintering aid it is necessary to realise high temperatures above 1650°C for achieving a density of ≥ 90%. In glycine-nitrate combustion synthesis process (section 4.1.1) only a density of 55.1% (of the theoretical density) was obtained. The reason for this low density can probably be found in connection with the sintering temperature in the furnace. As it later declared it was a temperature gradient of ± 50°C in the furnace. In the description of the method it was emphasised that the particle size of the starting powder must be less than 100nm[38]. This however may not be achieved with a ball mill because of, Si particles coming off of the equipment and contaminated the powder by longer milling at higher revolutions. Those will melt under the sintering process and led to the destruction of the sample.

For the second method NiO was used as sintering aid (section 4.1.2) and densities of 89% and 93% were reached introducing 1wt% and 2wt% NiO, respectively. Compared to other sintering aids, like ZnO and CuO, NiO showed similar effects in increasing the density and by increasing the amount of sintering aid the density further increased up to a certain point [35] [49]. NiO also has strong effects on the shrinking range, while Cu and Zn do not perform as well [35]. For clean samples free of reaming sintering aid use of $LiNO_3$ should be considered. This is because this compound evaporates completely during the sintering process [50].

6.2 Electrolyte

6.2.1 Temperature dependency of the conductivity

The conductivity of 20, 15 and 10% yttrium doped barium zirconate was found by impedance spectroscopy over the temperature range of 150 to 650°C. The deconvoluted results for bulk, grain boundary and the total- conductivity are displayed in section 5.2.

6.2.2 $BaZr_{0.9}Y_{0.1}O_{3-\delta}$

Under the experimental set the bulk conductivity of BYZ10 decreased with one order of magnitude when compared to experiments of H.G Bohn et al. [36] who described a sintering method without incorporating a sintering aid. Total conductivity measures was similar to conductivity results rapported by Ricote in $BaZr_{0.7}Ce_{0.2}Y_{0.1}O_{3-\delta}$ [51]. This is somehow unexpected because $BaZr_{0.7}Ce_{0.2}Y_{0.1}O_{3-\delta}$ as shown by Kreuer [29] was found to be a better conductor than $BaZr_{0.9}Y_{0.1}O_{3-\delta}$.

For temperatures >350°C the specific grain boundary was 5 orders of magnitude lower than the bulk conductivity. This difference was decreasing with higher temperatures, but at the temperature range measured, it was the grain boundary which had the lowest conductivity in wet conditions.

The activation energies were calculated from equation (2.3) and it is seems that the Arrheniusplot had different linear behaviours, one at the temperature range between 100-350°C and the second from 450- 650°C. The low temperature activation energy for the grain boundaries had a value of 0.73eV while the high temperatures range had an activation energy of 0.80eV. The differences diminished to eventually became negligible. The same applies for the bulk, where the activation energy was almost the same. The total activation energy for the grain boundary is 0.80eV which indicates protonic conductivity. This means that the increase of the conductivity is correlated with the increasing protonic conductivity [36]. The bulk conductivity had a activation energy of 0.44eV for the highest temperature range which confirm the activation energy measured by Kreuer how who reported similar values [15]. For the low temperature range and the total activation energy they were calculated to be 0.36eV and 0.33eV, respectively.

Table 6.1: Activation energies for $BaZr_{0.9}Y_{0.1}O_{3-\delta}$

	Bulk interior			Grain boundary			Total		
	300-650°C	100-350°C	100-650°C	350-650°C	100-350°C	100-650°C	350-650°C	100-350°C	100-650°C
E_a [eV]	0.44	0.36	0.33	0.8	0.73	0.8	0.46	0.60	0.53

6.2.3 $BaZr_{0.9}Y_{0.1}O_{3-\delta}$ oxygen dependency

The pO2-dependency of σ_{total} was almost nil (slope of 0.01) at 450°C. According to the Brouwer-diagram (section 2.6), none of the defects concentration changes were close to this slope. Therefor it can be anticipated that there is no oxygen dependency at this temperature. At higher temperatures however this may change. Nonetheless, σ_{Bulk} and σ_{Gb} had different pO_2-dependencies. The dependency of the bulk conductivity is independent of the oxygen partial pressure. The grain boundary conductivity on the other hand had a more significant slope of 0.05. This is still little, but a similar dependency was deduced form the pO_2 measurements of the electrolyte in the electrode part of this thesis, section 5.5.2. For this, the atmospheric conditions were the same, while the temperature was raised to 650°C. It is also notable that the electrolyte had a Y content of 20 mol%, and that the conductivity measured was the combined bulk- and grain boundary conductivity.

A positive pO_2-dependency means that the conductivity consists of oxygen vacancies and electron holes see equation (2.31). In fact oxygen will diffuse into the vacancies to create electron holes, which than becomes the predominant charge carrier. Similar results are shown in the literature however for higher temperature [52, 53].

6.2.4 $BaZr_{0.9}Y_{0.1}O_{3-\delta}$ water vapour dependency

The total conductivity is shown in Figure 5.11 at 600°C. The data plotted were obtained from impedance spectroscopy, ensuring that only the electrolyte contribution was considered. With decreasing water content the equilibrium (2.30) is shifted to the left and more oxygen vacancies are created. According to Figure 2.6 it can be anticipated that this increase of conductivity is from an increase of electron holes or oxygen vacancy concentrations. Comparing the slopes of the pH_2O-dependencies for oxygen vacancies and electron holes it is however more likely that

rather the electron hole concentration than the oxygen vacancies is increasing. This can probably be explained by the pH_2O-dependency measured (-0.26) which was closer to the p-type dependency of (-0.5) than to oxygen vacancies (water vapour dependency on concentration of -1). A similar behaviour is shown in the literature, where the conductivity between wet and dry conditions were different by an order of magnitude [54].

It is also suggested that in BYZ10 with NiO as a sintering aid, the high p-type conductivity can be explained from the introduction of new oxidation states. Nickel in the material will create oxygen vacancies and according to equation (2.31) more electron holes will be created in oxidising conditions [51]. Another indicator for p-type conductivity is the pO_2-dependency. As shown in Figure 5.9, the conductivity for the grain boundary was increasing with pO_2. From the equilibrium (2.31) it may appear that the electron hole contribution to the conductivity increases. One the other hand, this behaviour is opposite of the common understanding of BYZ10%. Literature for BYZ10% without NiO suggests that, depending on the conditions, the total conductivity decreases with the falling of pH_2O which can be a result of lower proton concentrations leading to lower the proton conductivity [43].
Other studies [55] suggest that the proton conductivity is dominating in a temperature range T $\leq$450°C while at temperatures above oxygen vacancies are dominating the conductivity.

6.2.5 $BaZr_{0.85}Y_{0.15}O_{3-\delta}$

The bulk and grain boundary showed a change in activation energy at 400°C, while the total conductivity remained unchanged. For the bulk the differences between high and low temperatures were only 0.07eV which can be cause of noise or data errors in the fitting results. It was therefore reasonable to make a linear regression over the entire temperature interval to find the activation energy of the bulk, which eventually was calculated as 0.37eV.
For the grain boundary the activation energy almost doubled with rising temperatures. For the low temperatures the activation energy of 0.78eV was similar to the proton activation energy reported in literature, while an activation energy of 1.45eV was indicating electron hole conductivity [56]. This further substantiated the statements above ware the pH_2O-dependencies measured at 600°C also showed p-type conductivity.

The conductivity was one order of magnitude lower than BZY15 measurements reported by Tong et al. [57]. Also in this study, E_a for bulk conductivity changed at temperatures above 450°C, although only bulk conductivity not the grain boundary was considered.

The total activation energy of 0.50eV indicates that protons are the dominating charge carrier over the entire temperature range.

Table 6.2: Activation energies for $BaZr_{0.,85}Y_{0.,15}O_{3-\delta}$

	Bulk interior			Grain boundary			Total		
	400-600°C	100-400°C	100-600°C	400-600°C	100-400°C	100-600°C	400-650°C	100-400°C	100-600°C
Ea eV	0.38	0.31	0.37	1.45	0.78	0.76	0.48	0.57	0.50

6.2.6 $BaZr_{0.8}Y_{0.2}O_{3-\delta}$

The total conductivity measured was similar to the results reported by Haile [58]. The activation energies for the bulk, grain boundary and for the total electrolyte was also at a similar level.
It should be stated that this sample showed shifts of activation energies similar to the 10% and 15% yttrium doped barium zirconate. There was a slight difference between the activation energies above and below 450°C. Altogether the activation energy shift for the bulk was small while the E_a for the grain boundary showed a bigger shift. It could be speculated that the shift reflects increase of electron holes, as described in the previous section.

Table 6.3: Activation energies for $BaZr_{0.8}Y_{0.2}O_{3-\delta}$

	Bulk interior			Grain boundary			Total		
	450-600°C	100-450°C	100-600°C	350-650°C	100-350°C	100-600°C	450-600°C	100-450°C	100-600°C
Ea eV	0.64	0.44	0.46	1.07	0.60	0.66	0.72	0.55	0.55

6.2.7 Comparison between 10%, 15%, and 20% yttrium doped barium zirconate

It was expected that 20% yttrium doping results in the highest proton conductivity, due to more vacancies developing, which subsequently hydrate and form hydroxide ions (equilibrium (2.32), (2.30)).

In this work, BYZ10 showed a similarly high total conductivity as BYZ20 under identical atmospheric conditions Figure 5.12a. This can be explained with the sintering process. By using sintering aid, smaller grain sizes are realise, and as a consequence, higher resistance is achieved. It may occur that a 10% yttrium doped sample does not show this effect and, BYZ10 has larger grains and thus fewer grain boundaries which are most resistive. This higher conductivity in BYZ10 is probably derived from the specific grain boundary resistance, which is higher than in BYZ20 sample.

As expected, the 20% yttrium doping showed higher conductivity than the 15% yttrium doped sample. But it is notable that both samples have a very similar grain boundary resistance (Figure 5.12c). Considering the specific grain boundary (Figure 5.12d) resistance is appears that the 15% doped sample had the highest conductivity which is most likely due to its grain size.

The Schottky barrier height is shown in Figure 5.13. For the BYZ 10 sample the calculated values were similar to the literature values reported by Kjølseth [7]. According to the space charge theory, the Schottky-height should decrease with increasing doping concentration, because more yttrium accumulates in the grain boundaries. This was shown for BYZ15, which had a lower gran boundary height than BYZ10. In contrast, the BYZ20 sample showed an increase of the Schottky-height with increasing temperature and this is opposite to what is proposed in the literature [7] [39].

6.3 Electrode polarization

6.3.1 Middle frequencies range

The logarithmic polarization resistance showed a linear behaviour in the temperature range between 500-650°C. The pseudo capacitance related to each impedance arc was calculated. When the resistance for the electrolyte was removed, the cathode showed two semi circles at the middle and low frequency range. The middle frequency range pseudo capacitance was calculated using the formula (2.23) with a value of $C \sim 10^{-5} F/cm^2$. This is in the range of the capacitance values for the charge transfer reaction reported by Dailly et al. [44], and renders the reaction process independent from the materials used. The results showed a decreasing capacitance, from $\sim 6*10^{-6} F/cm^2$ to $\sim 8*10^{-5} F/cm^2$, with increasing temperature. This seems to be a normal behaviour for a middle frequency reaction and has commonly stated in literature [44]. The mf semi-circles can be assigned to the charge transfer reaction according to Dailly [59].

On the other hand, the charge transfer should be independent of the pO_2. The dependency of 0.19 was close to the theoretical value of the oxygen diffusion process with a pO_2-dependency of (0.25), described in reaction step 3 and in reaction step 4 (pO_2-dependency of 0.125) in section 2.7. The deviation of the slope was somewhat larger, but the transmission of one electron to the oxygen ion in the three phase boundary happens fast, which could explain the low capacity.

From the logarithmic resistance arising from the mf semi-circle showing a linear behaviour in the temperature range considered, it was possible to calculate the activation energy from the slope of the Arrhenius plot (Figure 5.20). The value obtained in this study was 0.94eV as shown in Table 5.4. This is an indication for oxygen-ion transport to the TPB [20]. The activation energy values for migration of protons to the three phase would be significant lower with a activation energy of ~0.6eV [42].

The raw data of the water vapour dependency of polarization resistance didn't allow a differentiation into in middle and low range frequencies, and will therefore be discussed further in the total polarisation section 6.3.3.

6.3.2 Low frequency range

The low frequency semicircle could be distinguished from the middle frequency semicircle in the temperature range 500-650°C. In temperature range a Gerischer-element was used to represent the low frequency impedance in the equivalent circuit.

Thus, it was not possible to calculate the pseudo capacitance like in, section 2.3.4. To get a rough estimation of the capacitance value, the low frequency semi-circle was also fitted to an (RQ)-circuit element. This enabled the calculation of pseudo capacitance by formula (2.23). The calculated values are in range of 0.4-5.1F/cm^2 as shown in Table 10.2. This is one magnitude higher than the oxygen adsorption/desorption suggest in the literature, which rapport a pseudo capacitance of 10^{-1}F/cm^2 [43]. The (RQ) deconvolution of the low frequency part does not reflect the nature of the impedance sweep well, and the calculated pseudo capacitance can contain some errors in the values. However, the low frequency pseudo capacity is assigned the physical process of oxygen adsorption/dissociation on the electrode surface. Further, the activation energy for the lf process has been calculated for the linear behaviour of the Arrhenius-plot, Figure 5.20. The activation energy of 1.34eV is close to the value reported for the oxygen adsorption by He et al. [20], where the activation energy for the similar low frequency polarization was estimated to be 1.2eV for $Sm_{0.5}Sr_{0.5}CoO_{3-\delta}$. For further estimations the oxygen dependency has to be considered. As shown in Figure 5.24, the logarithmic lf polarisation resistance has an oxygen partial dependency of 0.43. This is in between the pO2-dependency of reaction step 1 and reaction step 2 presented in Table 2.2 in section 2.7. Step 1 is the oxygen adsorption and desorption on the electrode surface with a pO_2-dependency of 0.5, while step 2 is according to the first ionization of the adsorbed oxygen atom with a pO_2-dependency of 0.375. Since these values just are theoretical values, it could be that the low frequency semi-circle corresponds to either the oxygen adsorption or electron transfer. Most probity, will the low frequency polarization resistance correspond to both, adoption and transfer. High capacities as seen for the lf could also respond to the gas diffusion in between the open pores of the electrode. However, this processes should have a pO_2-dependency of 1.

6.3.3 Total frequency range

The sum of the corresponding resistances R_{mf} and R_{lf} represent the polarization resistance R_{pol}. R_{pol} is linear over a wide temperature range. In humid air, the activation energy in the temperature range 500-900°C has been calculated from the Arrhenius plot. The estimated value is 119.31kJ/mol. This is comparatively lower than other studies suggested. On LSCM placed on yttria-stabilized zirconia, the total polarization resistance in air was measured to be 130kJ/mol [60]. This is somehow also lower than $La_{0.72}Sr_{0.18}MnO_{3-\delta}$, where the activation energy is observed to be 153kJ/mol [61].

For the water vapour dependency the polarization resistance increase with pH_2O. It is reported that the increasing polarization resistance with rising pH_2O can be caused by blocking adsorption places on the electrode surface. Water molecules attach to the surface, and thereby occupy the adoption places for the oxygen [62]. The pH_2O-dependencys it could not differentiate between R_{mf} and R_{lf}, and it therefore can be assumed that both of them contribute to the total polarization resistance. It is reported that R_{lf} can be strongly influenced by the ambient water with a positive dependency on pH_2O, while R_{mf} often shows a slighter negative pH_2O-dependency [43]. Shown in Table 10.1 and Table 10.2 are the polarisation resistance of R_{mf} and R_{lf}. Since R_{lf} is most resistive over the entire temperate range it is expected that R_{lf} will determine the R_{pol} pH_2O-dependency. Because R_{mf} have the opposite pH_2O-dependency compared to R_{lf}, it will lower the pH_2O-dependency of R_{pol}.

6.3.4 Total performance

For the total polarization resistance is reported in the literature at values of 6.7 Ωcm^{-2} at 700°C in wet reducing atmospheres [63]. The achieved total polarisation resistance of 10.69Ωcm^{-2} at 600°C is also relatively high. Because of the low activation energy, it would be reasonable that interface between the electrode and electrolyte has be improved. Boulfrad et al. [63] have previously shown that the electrode performance can be improved by pre-coting the LSCM, which could reduce the resistance by 1/6. Further the nano-structure of the interface could be improved. As seen in Figure 5.18, the LSCM has relatively big grains. By reducing the grain sixe the three phase boundary cold be expended and more reaction points created.

The impedance measurement is done in between Point A and Point B (Figure 6.1). When measuring, the current will pass through the resistor with the lowest resistivity. Figure 6.1 shows R4, which is a non-faradaic resistor, in parallel to the R1- R3, contribute to the electrolyte and electrode reaction processes, which are faradaic. When the electrolyte conducts electron holes, they will bypass all reaction steps though resistor R4, and the electronic conductivity of electrode and electrolyte is measured. This will lower the total polarisation resistance of the electrode and will not reflect the true polarization resistance.

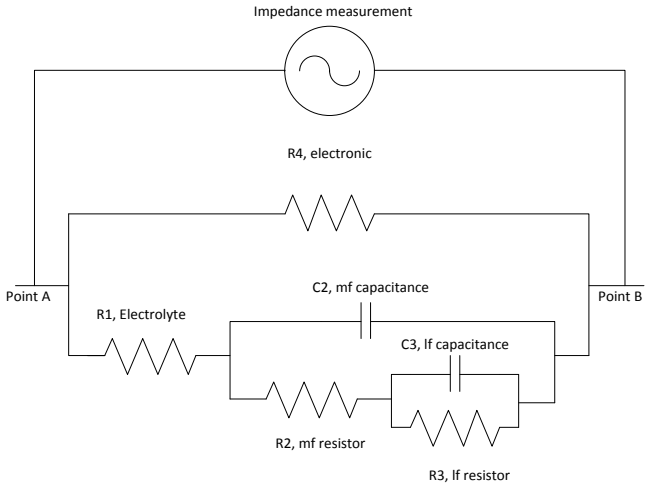

Figure 6.1: Total measurement where, R1,2,3 are faradaic resistance and R4 is non faradaic resistance.

6.4 Further work

In this thesis the main focus was to study conductivity. Further investigations are necessary to exploit the PC-SOFC processes.

It is rather evident that a high density electrolytes cannot be easily reached by wet chemical reaction sintering and it is therefore of high interest to study the effects of NiO on the total conductivity. Several pO_2- and pH_2O-dependencies have to be studied, to show if electron holes are dominating at high temperatures and to investigate whether shifts in, activation energy are attributed to proton losses. In the experiments reported here, BYZ10 and BYZ20 hads similar conductivities and it therefore remains to be investigated why BYZ20 expresses such a high

specific grain boundary resistance and Schottky-height. Still along the lines of BYZ20 characterisation, it remains to be investigated why LSM and LaCrO3 were incompatible with the BYZ20 sample.

Further investigation also needed to study grain boundaries more in details, especially to clarify why NiO did not improve the grain boundary conductivity. It is also crucial for the process to further our understanding of the crystal lattice mismatch. For this, TEM investigations should be done.

For a large scale fuel cell production, the sintering temperature is too high and the sintering times to long. It would therefore be highly desirable to further investigate how sintering temperatures and times can be reduced.

On the electrode side LSCM, the current-voltage dependency has to be investigated in order to determine the maximal power output. The electrode has still to undergo some modification and engineering to insure that longer three phase boundaries can be reached. It might be possible to pre-coat the electrode to lower the polarization resistance.

It can be highly interesting to build a working PC-SOFC. This can provide insights into rate limiting processes acting on the entire system. This further permits investigations on stability and performance and the comparison with other existing fuel cells like AFC, DMVC, MCFC, PAFC or SOFC.

7 Conclusion

The comparative analysis of the two sintering methods investigated in this study revealed that NiO as sintering aid catalyzes the formation of dense pellets and substantially lowers sintering temperatures. More dense pellets were formed by addition of 2wt% NiO compared to only 1wt% NiO. When NiO was used as sintering aid, BYZ10 had the biggest grain sizes while grains of BYZ20 were considerably smaller.

Impedance measurements for BYZ10 and BYZ20 revealed similar the total conductivity in wet air while the total conductivity of BYZ15 was lower by a half magnitude. The bulk conductivity was highest for BYZ10 at low temperature, while in contrast the conductivity of BYZ20 was highest conductivity at high temperatures. BYZ15 had the highest specific grain boundary conductivity followed by BYZ10 while the specific grain boundary conductivity of BYZ20 was lover to 1.5 order of magnitudes. Furthermore BYZ10, BYZ15, and BYZ20 showed different activation energies for high and low temperatures. The activation energy was assigned to electron hole conduction at temperatures above 450°C, while proton conductivity was dominating at lower temperatures.

On the electrode only LSCM proved compatible with BYZ20 as electrolyte. The polarization resistance of the middle frequencies could be assigned to oxygen-ion transport to the TPB with a resistance of 3.85Ωcm^{-2}, at 600°C in humid air. The low frequency range was found contributing to the oxygen adsorption and desorption on the electrode surface with a resistance of 6.38 Ωcm^{-2}, in wet air atmosphere and at temperatures of 600°C.

The total polarization resistance of $10.68 \Omega cm^{-2}$ at 600°C is acceptable when considering the preparation methods. By modifying the electrolyte electrode interface higher results can be obtained. Pre-coating of electrode surface might contribute to further reduce the resistance.

8 Bibliography

1. Boden, T.A., G. Marland, and R.J. Andres, *Global, Regional, and National Fossil-Fuel CO2 Emissions.* . 2012.
2. Norby, K.a., *Defects and Transport in Crystalline Solids* 2012.
3. Haile, S.M., D.L. West, and J. Campbell, *The role of microstructure and processing on the proton conducting properties of gadolinium-doped barium cerate.* J. Mater. Res., 1998. **13**(6): p. 1576-1595.
4. Haile, S.M., G. Staneff, and K.H. Ryu, *Non-stoichiometry, grain boundary transport and chemical stability of proton conducting perovskites.* Journal of Materials Science, 2001. **36**(5): p. 1149-1160.
5. De Souza, R.A., *The formation of equilibrium space-charge zones at grain boundaries in the perovskite oxide SrTiO3.* Physical Chemistry Chemical Physics, 2009. **11**(43): p. 9939-9969.
6. Guo, X. and R. Waser, *Electrical properties of the grain boundaries of oxygen ion conductors: Acceptor-doped zirconia and ceria.* Progress in Materials Science, 2006. **51**(2): p. 151-210.
7. Kjølseth, C., et al., *Space–charge theory applied to the grain boundary impedance of proton conducting BaZr0.9Y0.1O3 − δ.* Solid State Ionics, 2010. **181**(5–7): p. 268-275.
8. Gerischer, H., *Alternating-current polarization of electrodes with a potential-determining step for equilibrium potential.* Z. physik. Chem., 1951. **198**: p. 286-313.
9. Boukamp, B.A. and H.J.M. Bouwmeester, *Interpretation of the Gerischer impedance in solid state ionics.* Solid State Ionics, 2003. **157**(1–4): p. 29-33.
10. R.U. Atangulov, I.V.M., Solid State Ionics, 1993. **67**(9).
11. Adler, S.B., *Mechanism and kinetics of oxygen reduction on porous La1−xSrxCoO3−δ electrodes.* Solid State Ionics, 1998. **111**(1–2): p. 125-134.
12. Kröger, F.A. and H.J. Vink, *Relations between the Concentrations of Imperfections in Crystalline Solids*, in *Solid State Physics*, S. Frederick and T. David, Editors. 1956, Academic Press. p. 307-435.
13. Susumu Imashuku, T.U., Yoshitaro Nose, and Yasuhiro Awakura, *To Journal of Phase Equilibria and Diffusion Phase Relationship of the BaO-ZrO2-YO1.5 System at 1500 and 1600 ・C.* Phase Equilibria and Diffusion Phase, 2010.
14. Ishihara, T., *Perovskite Oxide for Solid Oxide Fuel Cells*. 2009, Boston, MA: Springer US.
15. Kreuer, K. and Kreuer, *Proton conducting alkaline earth zirconates and titanates for high drain electrochemical applications.* Solid State Ionics, 2001. **145**(1-4): p. 295.
16. van, H.F.H. and H.J.M. Bouwmeester, *Electrode properties of Sr-doped LaMnO3 on yttria-stabilized zirconia. II. Electrode kinetics.* J. Electrochem. Soc., 1997. **144**(1): p. 134-140.
17. van Hassel, B.A., B.A. Boukamp, and A.J. Burggraaf, *Electrode polarization at the Au, O2 (g) / yttria stabilized zirconia interface. Part II: electrochemical measurements and analysis.* Solid State Ionics, 1991. **48**(1–2): p. 155-171.

18. van Hassel, B.A., B.A. Boukamp, and A.J. Burggraaf, *Electrode polarization at the Au, O2(g)/yttria stabilized zirconia interface. Part I: Theoretical considerations of reaction model.* Solid State Ionics, 1991. **48**(1–2): p. 139-154.
19. Kim, J.-D., et al., *Characterization of LSM–YSZ composite electrode by ac impedance spectroscopy.* Solid State Ionics, 2001. **143**(3–4): p. 379-389.
20. He, F., et al., *Cathode reaction models and performance analysis of Sm0.5Sr0.5CoO3−δ–BaCe0.8Sm0.2O3−δ composite cathode for solid oxide fuel cells with proton conducting electrolyte.* Journal of Power Sources, 2009. **194**(1): p. 263-268.
21. Adler, S., *Factors Governing Oxygen Reduction in Solid Oxide Fuel Cell Cathodes.* Chemical reviews, 2004. **104**(10): p. 4791.
22. http://www.fuelcelltoday.com/about-fuel-cells/history#Origins, *Origins of Fuel Cell.* 2012.
23. H. v. Wartenberg, H.W., *Schmelzdiagramme höchstfeuerfest Oxyde.* Zeitschrift für anorganische und allgemeine Chemi (ZAAC), 1930. **190**(1).
24. Naray-Szabo, S.v., *Der Strukturtyp des Perowskites* Die Naturwissenschaft, 1943.
25. Gränicher, v.H., *Dielelktrische Eigenschaften von Substanzen des Perwskittypes.* Helvetica Physica Acta, 1951. **24**.
26. H. Iwahara, T.E., H. Uchida, N.Maeda, *Proton conduction in Sintered Oxides an its application to steam electrolysis for hydrogen productoin.* Solid State Ionics, 1981.
27. Talib, I.A.L., Mouloud; Omar, Ramli, *Study of proton conduction in yttrium-doped BaZrO3 at high temperature.* Solid State Ionics: Materials and Deevices, 2000: p. 559.
28. Lemmens, M.J.a.P., *Crystallography and Chemistry of Perovskites.* 2005.
29. Kreuer, K.D., *Proton-conducting oxides.* Annu. Rev. Mater. Res., 2003. **33**: p. 333-359.
30. Norby, T., et al., *Hydrogen in oxides.* Dalton Transactions, 2004. **0**(19): p. 3012-3018.
31. Kreuer, K.D., *On the development of proton conducting materials for technological applications.* Solid State Ionics, 1997. **97**(1–4): p. 1-15.
32. Kreuer, K.D., *Aspects of the formation and mobility of protonic charge carriers and the stability of perovskite-type oxides.* Solid State Ionics, 1999. **125**(1–4): p. 285-302.
33. Bjørheim, T.S., et al., *A combined conductivity and DFT study of protons in PbZrO3 and alkaline earth zirconate perovskites.* Solid State Ionics, 2010. **181**(3–4): p. 130-137.
34. LÜ, J., et al., *Chemical stability of doped BaCeO3-BaZrO3 solid solutions in different atmospheres.* Journal of Rare Earths, 2008. **26**(4): p. 505-510.
35. Babilo, P. and S.M. Haile, *Enhanced Sintering of Yttrium-Doped Barium Zirconate by Addition of ZnO.* Journal of the American Ceramic Society, 2005. **88**(9): p. 2362-2368.
36. T.Schober, H.G.B.a., *Electrical Conductivity of the High‐Temperature Proton Conductor BaZr0.9Y0.1O2.95.* Journal of the American Ceramic Society, 2000. **83**(4): p. 768-772.
37. Schober, T. and H.G. Bohn, *Water vapor solubility and electrochemical characterization of the high temperature proton conductor BaZr0.9Y0.1O2.95.* Solid State Ionics, 2000. **127**(3–4): p. 351-360.
38. Babilo, P., *Processing of yttrium-doped barium zirconate for high proton conductivity.* Journal of materials research, 2007. **22**(05): p. 1322.
39. Kjølseth, C., *Personal conversation* 2013.
40. Iguchi, F., et al., *Microstructures and grain boundary conductivity of BaZr1−xYxO3 (x = 0.05, 0.10, 0.15) ceramics.* Solid State Ionics, 2007. **178**(7–10): p. 691-695.
41. Quarez, E., K.V. Kravchyk, and O. Joubert, *Compatibility of proton conducting La6WO12 electrolyte with standard cathode materials.* Solid State Ionics, 2012. **216**(0): p. 19-24.
42. Ricote, S., et al., *Microstructure and performance of La0.58Sr0.4Co0.2Fe0.8O3−δ cathodes deposited on BaCe0.2Zr0.7Y0.1O3−δ by infiltration and spray pyrolysis.* Journal of Power Sources, 2012. **209**(0): p. 172-179.

43. Ricote, S., et al., *LaCoO3: Promising cathode material for protonic ceramic fuel cells based on a BaCe0.2Zr0.7Y0.1O3−δ electrolyte.* Journal of Power Sources, 2012. **218**(0): p. 313-319.
44. Dailly, J., et al., *Perovskite and A2MO4-type oxides as new cathode materials for protonic solid oxide fuel cells.* Electrochimica Acta, 2010. **55**(20): p. 5847-5853.
45. Zongping Shao, S.M.H., *A high-performance cathode for the next generation of solid-oxide fuel cells.* Materials Science, California Institute of Technology, 2004.
46. Tong, J., et al., *Solid-state reactive sintering mechanism for large-grained yttrium-doped barium zirconate proton conducting ceramics.* Journal of Materials Chemistry, 2010. **20**(30): p. 6333-6341.
47. J, Č.N.e.a., Electrochem. Soc, 2012. **159**: p. F461-F467.
48. Boukamp, B.A., *Equivalent Curcuit for Windows.* University of Twente/WisseQ, Enschede, 2003.
49. Gao, D. and R. Guo, *Structural and electrochemical properties of yttrium-doped barium zirconate by addition of CuO.* Journal of Alloys and Compounds, 2010. **493**(1–2): p. 288-293.
50. Sun, Z., et al., *Lowering grain boundary resistance of BaZr0.8Y0.2O3-[small delta] with LiNO3 sintering-aid improves proton conductivity for fuel cell operation.* Physical Chemistry Chemical Physics, 2011. **13**(17): p. 7692-7700.
51. Ricote, S. and N. Bonanos, *Enhanced sintering and conductivity study of cobalt or nickel doped solid solution of barium cerate and zirconate.* Solid State Ionics, 2010. **181**(15–16): p. 694-700.
52. Park, H.J., *Electrical properties of the protonic conductor 1 mol% Y-doped.* J. Solid State Electrochem., 2011. **15**(10): p. 2205-2211.
53. Nomura, K. and H. Kageyama, *Transport properties of Ba(Zr0.8Y0.2)O3 − δ perovskite.* Solid State Ionics, 2007. **178**(7–10): p. 661-665.
54. Patnaik, A.S. and A.V. Virkar, *Transport properties of potassium-doped BaZrO3 in oxygen and water vapor containing atmospheres.* ECS Trans., 2006. **1**(7, Solid State Ionic Devices IV): p. 347-356.
55. Pornprasertsuk, R., et al., *Proton conductivity of Y-doped BaZrO3: Pellets and thin films.* Solid State Sciences, 2011. **13**(7): p. 1429-1437.
56. Patnaik, A.S. and A.V. Virkar, *Transport properties of potassium-doped BaZrO3 in oxygen- and water-vapor-containing atmospheres.* Journal of the Electrochemical Society, 2006. **153**(7): p. A1397-A1405.
57. Tong, J., et al., *Electrical conductivities of nano ionic composite based on yttrium-doped barium zirconate and palladium metal.* Solid State Ionics, 2012. **211**(0): p. 26-33.
58. Yamazaki, Y., R. Hernandez-Sanchez, and S.M. Haile, *High Total Proton Conductivity in Large-Grained Yttrium-Doped Barium Zirconate.* Chem. Mater., 2009. **21**(13): p. 2755-2762.
59. Dailly, J., et al., *Electrochemical properties of perovskite and A 2MO 4-type oxides used as cathodes in protonic ceramic half cells.* Journal of Solid State Electrochemistry, 2011. **15**(2): p. 245-251.
60. Zhang, L., et al., *Characterization of doped La0.7A0.3Cr0.5Mn0.5O3 − δ (A = Ca, Sr, Ba) electrodes for solid oxide fuel cells.* Solid State Ionics, 2009. **180**(17–19): p. 1076-1082.
61. Jiang, S.P. and W. Wang, *Novel structured mixed ionic and electronic conducting cathodes of solid oxide fuel cells.* Solid State Ionics, 2005. **176**(15–16): p. 1351-1357.
62. Strandbakke, R., *From personal conversation, aboudt a unpublished paper.* 2013.
63. Boulfrad, S., et al., *Pre-coating of LSCM perovskite with metal catalyst for scalable high performance anodes.* International Journal of Hydrogen Energy, (0).

9 Appendix A

Her shown are the results of the de convolution with the EqC-software. This appendix is according to the temperature plots in section 5.2

Table 9.1: Results from fitting the data with EqC, BYZ20

	Bulk interior				Grain boundary			
T	R_1	Y_1	n_1	C_1	R_2	Y_2	n_2	C_2
[°C]	[Ωcm]	[Ω^{-1}]		[F/cm]	[Ωcm]	[Ω^{-1}]		[F/cm]
150	$1.65*10^{5}$	$8.30*10^{-11}$	0.79	$4.68*10^{-12}$	$7.87*10^{5}$	$2.69*10^{-07}$	0.53	$6.72*10^{-08}$
200	$4.33*10^{4}$	$2.76*10^{-10}$	0.73	$3.73*10^{-12}$	$1.25*10^{5}$	$6.78*10^{-07}$	0.51	$6.37*10^{-08}$
250	$1.49*10^{4}$	$6.59*10^{-11}$	0.83	$3.70*10^{-12}$	$3.29*10^{4}$	$2.39*10^{-06}$	0.44	$9.52*10^{-08}$
300	$6.44*10^{3}$	$5.15*10^{-11}$	0.80	$6.80*10^{-12}$	$8.27*10^{3}$	$5.84*10^{-06}$	0.44	$1.30*10^{-07}$
400	$1.07*10^{3}$				$1.13*10^{3}$	$8.79*10^{-05}$	0.33	$7.58*10^{-07}$
450	$8.82*10^{2}$				$5.59*10^{2}$	$8.14*10^{-05}$	0.4	$7.94*10^{-07}$
500	$2.50*10^{2}$				$1.44*10^{2}$	$3.89*10^{-10}$	1	$3.89*10^{-10}$
600	$1.16*10^{2}$				$2.36*10^{1}$	$4.02*10^{-09}$	1	$4.02*10^{-09}$

Table 9.2: Results from EqC fitting for BYZ15

	Bulk interior				Grain boundary			
T	R_1	Y_1	n_1	C_1	R_2	Y_2	n_2	C_2
[°C]	[Ωcm]	[Ω^{-1}]		[F/cm]	[Ωcm]	[Ω^{-1}]		[F/cm]
200	$7.04*10^{4}$	$2.69*10^{-11}$	0.95	$1.30*10^{-11}$	$3.65*10^{5}$	$3.77*10^{-07}$	0.31	$5.08*10^{-09}$
250	$4.02*10^{4}$	$1.02*10^{-09}$	0.66	$5.91*10^{-12}$	$4.81*10^{4}$	$2.29*10^{-07}$	0.51	$2.84*10^{-09}$
300	$2.50*10^{4}$	$1.27*10^{-07}$	0.36	$4.93*10^{-12}$	$7.07*10^{3}$	$1.63*10^{-07}$	0.69	$8.11*10^{-09}$
400	$5.22*10^{3}$				$9.42*10^{2}$	$4.51*10^{-09}$	0.92	$1.64*10^{-09}$
450	$2.40*10^{3}$				9.00*102	1.81*10-09	0.84	$7.79*10^{-10}$
500	$1.75*10^{3}$				2.34*102	7.79*10-10	1	$5.73*10^{-08}$
600	$7.18*10^{2}$				1.40E*101	5.73*10-08	1	$7.59*10^{-10}$

Table 9.3: Fitting results for EqC. BYZ10

	Bulk interior				Grain boundary			
T	R_1	Y_1	n_1	C_1	R_2	Y_2	n_2	C_2
[°C]	[Ωcm]	[Ω^{-1}]		[F/cm]	[Ωcm]	[Ω^{-1}]		[F/cm]
150	$1.38*10^{4}$	$2.83*10^{-09}$	0,71	$4.66*10^{-11}$	$1.26*10^{5}$	$1.95*10^{-07}$	0.62	$1.97*10^{-08}$
250	$1.03*10^{3}$	$1.00*10^{-12}$	1	$1.00*10^{-12}$	$8.87*10^{3}$	$6.71*10^{-06}$	0.36	$4.58*10^{-08}$
350	$3.09*10^{2}$				$1.15*10^{2}$	$5.20*10^{-09}$	0.91	$1.34*10^{-09}$
450	$1.67*10^{2}$				$1.46*10^{1}$	$1.81*10^{-08}$	1.00	$1.81*10^{-08}$
550	$6.99*10^{1}$				$2.30*10^{-01}$	$1.77*10^{-06}$	0.95	$9.16*10^{-07}$
650	$2.78*10^{1}$				$7.09*10^{-01}$	$3.54*10^{-07}$	1.00	$3.54*10^{-07}$

10 Appendix B

Her shown are the results of the de convolution with the EqC-software. This appendix is according to the temperature plots in section 5.5.

Table 10.1: middle range polarization resistance, calculated in according to the Randle circuit section 2.3.4.

T	R_{mf}	Y_{mf}	N_{mf}	C_{mf}
[°C]	[Ωcm^2]	[Ω^{-1}]		[F/cm^2]
500	18.96	$1.04*10^{-3}$	0.39	$6.96*10^{-6}$
550	8.36	$2.32*10^{-3}$	0.39	$1.48*10^{-5}$
600	3.85	$6.02*10^{-3}$	0.36	$2.83*10^{-5}$
650	1.58	$1.25*10^{-2}$	0.38	$8.90*10^{-5}$

Table 10.2: low frequency polarization resistance, where the resistance R is calculated from formula (2.26)

T	R_{lf}	Y_{lf}	K_{lf}	C_{lf} (RQ)-fitting
[°C]	[Ωcm^2]	[$S^{-1}s^{0.5}$]	[s^{-1}]	[F/cm^2]
500	83.83	0.192	$3.86*10^{-3}$	$0.7*10^{+1}$
550	23.64	0.453	$8.75*10^{-3}$	$0.5*10^{+1}$
600	6.83	1.14	$1.65*10^{-2}$	$3.9*10^{+1}$
650	2.78	2.48	$2.1*10^{-2}$	$5.1*10^{+1}$

Table 10.3: (RQ)-fitting for 700 up to 900°C

T	R	Y	n	C
[°C]	[Ωcm^2]	[Ω^{-1}]		[F/cm^2]
700	0.60	$1.52*10^{-3}$	0.52	$3.23*10^{-4}$
800	0.14	$1.50*10^{-3}$	0.43	$2.63*10^{-3}$
900	0.04	$1.76*10^{-3}$	0.59	$9.81*10^{-3}$